

# INTERNAL AND EXTERNAL ALIGNMENT OF THE SHAPES AND ANGULAR MOMENTA OF $\Lambda$ CDM HALOS

JEREMY BAILIN<sup>1</sup> AND MATTHIAS STEINMETZ<sup>2,3</sup>

Steward Observatory, University of Arizona, 933 N Cherry Ave, Tucson, AZ 85721 USA  
and

Astrophysikalisches Institut Potsdam, An der Sternwarte 16, D-14482 Potsdam, Germany

*Draft version March 20, 2019*

## ABSTRACT

We investigate how the shapes and angular momenta of galaxy and group mass dark matter halos in a  $\Lambda$ CDM  $N$ -body simulation are correlated internally, and how they are aligned with respect to the location and properties of surrounding halos. We explore these relationships down to halos of much lower mass ( $10^{11} h^{-1} M_{\odot}$ ) than previous studies. The halos are triaxial, with  $c/a$  ratios of  $0.6 \pm 0.1$  and a mean two-dimensional projected ellipticity of  $\langle e \rangle = 0.24$ . More massive halos are more flattened. The axis ratios rise out to  $0.6 r_{\text{vir}}$ , beyond which they drop. The principal axes, in particular the minor axes, are very well aligned within  $0.6 r_{\text{vir}}$ . High mass halos show particularly strong internal alignment. The angular momentum vectors are also reasonably well aligned, though with more scatter. The angular momentum vectors tend to align with the minor axes and lie perpendicular to the major and intermediate axes. The properties of a halo at  $0.4 r_{\text{vir}}$  are quite characteristic of the properties at most other radii within the halo. There is a very strong tendency for the minor axes of halos to lie perpendicular to large scale filaments, and a much weaker tendency for the major axes to lie along the filaments. This alignment extends to much larger separations for group and cluster mass halos than for galaxy mass halos. The angular momenta of galaxy mass halos point parallel to filaments, while those of group and cluster mass halos show a very strong tendency to point perpendicular to the filaments. This suggests that group and cluster mass halos acquire most of their angular momentum from the accretion of subhalos along filaments, while the angular momentum in galaxy mass halos has retained some memory of the primordial tidal torques that acted on the halo during its formation.

*Subject headings:* galaxies: formation — galaxies: halos — galaxies: structure — dark matter — galaxies: clusters: general — methods: N-body simulations

## 1. INTRODUCTION

The three-dimensional structure of the dark matter halos that host galaxies, groups, and clusters is an important aspect of their nature that can provide insight into their formation and affect the luminous structures within. The orientation of the halo shapes and angular momenta, both internally and with respect to surrounding halos, provide important constraints on other studies of galaxy formation and evolution.

Halos formed in cosmological simulations are generally not spherical, but have an ellipsoidal shape. There have been several studies of the shapes of halos in low resolution  $N$ -body simulations based on the standard cold dark matter (CDM) paradigm (Frenk et al. 1988; Dubinski & Carlberg 1991; Warren et al. 1992 (hereafter W92); Cole & Lacey 1996). These studies have found that halos are usually triaxial, with a preference for prolate figures at small radii and more oblate figures at large radii, and have minor-to-major axis ratios ranging from 0.3 to almost unity. Dubinski & Carlberg (1991), in simulations of the formation of isolated galaxies where the effects of the external tidal field were prescriptively superimposed, found that the projected two-dimensional ellipticities peak around  $e = 0.5$ , where

$$e \equiv 1 - q, \quad (1)$$

for a projected axis ratio of  $q$ . W92 found that while this is true in the inner regions, the location of the peak falls to  $e = 0.25$  beyond 50 kpc. The behaviour of the axis ratios with radius is controversial; Dubinski & Carlberg (1991) and W92 find that the axis ratios increase (become more spherical) with radius, while Frenk et al. (1988) and Cole & Lacey (1996) find that they decrease with radius. W92 have also studied the internal alignment of the ellipsoid principal axes. They found that both the major and minor axes of halos are extremely well aligned out to 40 kpc.

More recently, several authors have performed large high resolution simulations using the currently-favoured  $\Lambda$ CDM cosmology (Bullock 2002; Jing & Suto 2002 (hereafter JS02); Kasun & Evrard 2004 (hereafter KE04)). Bullock (2002) finds that the  $c/a$  axis ratios are a strong function of halo mass, and range from 0.55 at  $10^{14} h^{-1} M_{\odot}$  to 0.7 around  $10^{12} h^{-1} M_{\odot}$ , with a distribution that is peaked but has a large tail to small axis ratios. He also finds that the inner  $30 h^{-1}$  kpc of halos are more spherical than the outer regions, i.e. the axis ratios decrease with radius. On the other hand, JS02 find  $c/a$  axis ratios that increase with radius, decrease slightly with mass, and are well fit by a Gaussian centred at  $c/a = 0.55$  with a width of 0.11. They find that the major axes of halos are relatively well aligned — typically  $\cos \theta_{11} \sim 0.8$ , where  $\theta_{11}$  is the angle between the major axis at small or large radius compared to that at an intermediate radius. The alignment of the middle axes

<sup>1</sup> jbailin@as.arizona.edu

<sup>2</sup> msteinmetz@aip.de

<sup>3</sup> David and Lucile Packard Fellow

is somewhat poorer, but JS02 argue that this is due to the inclusion of nearly prolate halos whose axes are degenerate and therefore not well determined. KE04 find more spherical shapes in their very large sample of high mass halos ( $M > 3 \times 10^{14} h^{-1} M_{\odot}$ ), possibly due to the spherical outer boundary they impose, with  $c/a \approx 0.65$ .

The shapes of dark matter halos can have important observational consequences (for a good review, see Sackett 1999). On galactic scales, they can affect the coherence of tidal streams. Some authors have claimed that the thinness of the tidal stream associated with the Sagittarius dwarf spheroidal indicates that the halo of the Milky Way is nearly spherical, with  $c/a \gtrsim 0.8$  (Ibata et al. 2001; Majewski et al. 2003; Martínez-Delgado et al. 2004). However, more recent studies suggest that the material that makes up the stream was stripped from the satellite too recently to have had time to undergo differential precession, which severely weakens the constraints on the halo shape (Helmi 2004a,b). Helmi (2004b) claims that the stream is best fit by a prolate halo elongated perpendicular to the disk with  $c/a \approx 0.6$ , while Johnston, Law, & Majewski (2004) have compared the precession of the leading stream to the trailing stream and claim an oblate halo with  $c/a \sim 0.83 - 0.92$  provides the best fit. Other measures of the Milky Way ellipticity using the flaring of the gas disk at large radius or the anisotropy of stellar velocities suggest that the halo is oblate with a flattening of  $c/a \sim 0.8$  (Olling & Merrifield 2000). The shapes of the halos of external galaxies can be measured using the flaring of the gas layer (Olling & Merrifield 2000), the projected shape of X-ray gas (Buote et al. 2002), or the kinematics of polar ring galaxies (Sackett et al. 1994). These methods suggest that galaxy halos have a wide range of flattenings from  $c/a \sim 0.3 - 0.8$ . A new method for measuring the shapes of external galaxy halos is weak gravitational lensing. By measuring the azimuthal variation of the shear with respect to the position angle of the visible lens galaxy (Natarajan & Refregier 2000), Hoekstra, Yee, & Gladders (2004) detected an average projected halo ellipticity of  $\langle e \rangle = 0.33$  for halos with an average mass of  $8 \times 10^{11} h^{-1} M_{\odot}$ . This detection also implies that the orientation of the visible and dark mass in galaxies must be similar. On group and cluster scales, X-ray observations and the Sunyaev-Zeldovich effect can be directly used as a probe of halo ellipticities (Lee & Suto 2003, 2004).

The orientation of the angular momentum in halos has also been studied in cosmological numerical simulations. Early low-resolution studies (Barnes & Efstathiou 1987; Frenk et al. 1988; Cole & Lacey 1996) gave conflicting results due to the difficulty of measuring the direction of the angular momentum with few particles. Other CDM studies (Dubinski 1992; W92) have found that the direction of the angular momentum at different radii is usually the same, but that the distribution of alignments has a tail that stretches all the way to anti-alignment. This result is verified by recent high-resolution  $\Lambda$ CDM simulations (Bullock et al. 2001). CDM studies have also found that the angular momentum is most often aligned with the minor axis and perpendicular to the major axis, although there is some scatter (Dubinski 1992; W92). This result has not yet been thoroughly tested in high-resolution  $\Lambda$ CDM simulations.

Internal misalignment of the angular momentum can have a number of observational consequences. It may cause galactic warps (Ostriker & Binney 1989; Debattista & Sellwood 1999; López-Corredoira, Betancort-Rijo, & Beckman 2002; Bailin 2003), or manifest itself in anisotropic distributions of the orbits of satellite galaxies (Holmberg 1974; Zaritsky et al. 1997; Aubert, Pichon, & Colombi 2004; Knebe et al. 2004).

Going beyond individual halos, the shapes and angular momenta of nearby halos can be correlated due to initial conditions or dynamical evolution. This subject has attracted increased interest recently due to the emergence of weak gravitational lensing as a method to measure the projected mass density in front of background galaxies. Intrinsic correlations between the projected shapes of luminous galaxies act as spurious background signals in weak lensing, so predicting their magnitude is important. At a more fundamental level, the degree of correlation between structures can be tested against models, and can inform our understanding of the origin of halo shapes and angular momenta.

Measurements of halo alignments and correlations come from two sources: cluster orientations and large galaxy surveys. The study of the alignment of cluster orientations was pioneered by Binggeli (1982), who used the locations of the constituent galaxies to determine that the major axes of clusters separated by less than  $15 h^{-1}$  Mpc tend to point toward each other. While some authors have not found any such correlation (e.g. Struble & Peebles 1985), larger samples of both galaxies and clusters, along with improved error estimates, have confirmed this result (e.g. Flin 1987; Rhee & Katgert 1987; Plionis 1994). The cluster potential is better probed by X-ray emitting gas (Sarazin 1986; Lee & Suto 2003, 2004). While early studies using X-ray contours found no alignment of clusters with the large scale structure (Ulmer, McMillan, & Kowalski 1989), more and better data have confirmed that the orientation of both the substructure and the main cluster potential tends to point toward neighbouring clusters (West, Jones, & Forman 1995; Chambers, Melott, & Miller 2002).

While the principal axes of clusters can be determined from optical or X-ray photometry, the angular momentum direction is very difficult to determine. In disk galaxies, on the other hand, the angular momentum direction of the baryons, presumed to be perpendicular to the orientation of the disk, can be measured much more easily than the shape of the dark matter halo. Although there may be some misalignment between the angular momentum of the baryons and dark matter (van den Bosch et al. 2002; Sharma & Steinmetz 2004), spiral galaxies still provide the best targets for looking for angular momentum alignments and correlations. Studies with small samples of spiral galaxies (less than a few hundred) have generally found no correlation between the orientation of the angular momentum and the large scale structure (Han, Gould, & Sackett 1995; Cabanela & Dickey 1999; see however Navarro, Abadi, & Steinmetz 2004). With a sample of 618 lenticular and disk galaxies in the local supercluster, Kashikawa & Okamura (1992) found that while the full sample was consistent with an isotropic

distribution of angular momenta, those galaxies within  $2 h^{-1}$  Mpc of the supergalactic plane tend to have spin vectors pointing in the plane, while those above or below the plane tend to have spin vectors that point toward or away from the plane. Navarro et al. (2004) also find a clear excess of galaxies whose angular momenta lie in the supergalactic plane. Larger samples of galaxies provide further evidence of alignments between spin and the large scale structure: Pen, Lee, & Seljak (2000) have found that the spin directions of the 12,122 spiral galaxies in the Tully catalog are positively correlated at separations less than  $3 h^{-1}$  Mpc, while Brown et al. (2002) have measured intrinsic alignments between galaxy orientations at a range of angular separations in the  $2 \times 10^6$  galaxies of the SuperCOSMOS survey.

Many recent theoretical studies of halo alignment have been motivated by predicting the intrinsic alignment signal for weak lensing measurements. These studies jump straight to correlations of the ellipticities of luminous galaxies as a function of angular separation on the sky (e.g. Croft & Metzler 2000; Heavens, Refregier, & Heymans 2000; Catelan, Kamionkowski, & Blandford 2001; Crittenden et al. 2001). While these studies are useful for those making weak lensing observations, they do not provide any direct measurement of the intrinsic spatial alignments that can provide physical insight into the galaxy formation process.

Linear tidal torque theory (Doroshkevich 1970; White 1984) can be used to predict the directions of the angular momentum vectors and their correlations with the surrounding structure (Pen et al. 2000; Lee & Pen 2000, 2001; Porciani, Dekel, & Hoffman 2002a,b). These studies have found that the angular momenta of halos tend to lie perpendicular to the large scale structure, and that the correlation of the halo spin vectors with each other exists but is very weak. However, Porciani et al. (2002a) have tested the predictions of tidal torque theory against  $N$ -body simulations and have found that the spin directions of  $N$ -body halos show significant misalignment compared to the tidal torque predictions, with a mean misalignment of  $\sim 50^\circ$  at  $z = 0$ . Therefore,  $N$ -body simulations that take the full non-linear dynamics into account are necessary.

Some early numerical work at predicting the intrinsic alignments using simulations with power law or CDM power spectra found that the major axes of cluster mass halos tend to point toward other nearby clusters over scales of  $\sim 15 h^{-1}$  Mpc, and that there is a very weak tendency for the major axes to be correlated with each other over the same range of separations (Barnes & Efstathiou 1987; West, Villumsen, & Dekel 1991; van Haarlem & van de Weygaert 1993; Splinter et al. 1997). More recent high resolution  $N$ -body simulations in a  $\Lambda$ CDM cosmology have been studied to search for alignments of the major axes (Onuora & Thomas 2000; KE04), the angular momentum vectors (Hatton & Ninin 2001), or both (Faltenbacher et al. 2002; hereafter F02). These studies have found a strong tendency for the major axes of cluster mass halos to point toward other clusters out to several tens (or even hundreds) of Mpc and to correlate with each other out to  $20 h^{-1}$  Mpc. The situation for the angular momentum is murkier. Hatton & Ninin

(2001) have found that the angular momenta of halos tend to lie parallel to the large scale structure, while F02 have found that they lie perpendicular to the large scale structure, in agreement with the prediction from the linear theory (Lee & Pen 2001). Correlations of halo angular momentum vectors with each other are weak at best.

In this paper, we present an extensive study of the shapes of galaxy and group-mass halos in a large high resolution  $\Lambda$ CDM  $N$ -body simulation. We study the internal alignments of all of the principal axes and the angular momentum. We also study the alignment of all of these quantities with the large scale structure, and how they are correlated in halos of different separations. This work improves upon earlier studies of the internal structure of halos by using large high resolution simulations in a currently-favoured  $\Lambda$ CDM cosmology, by studying both the alignment of the angular momentum and the shape, and by using a method that allows us to quantify our errors and therefore feel confident about the source of any measured misalignments. Previous external alignment studies have all been restricted to massive clusters; we improve upon this significantly by reaching down to galaxy mass halos, by studying the mass dependence of the correlations, by studying the alignments of both the principal axes and the angular momenta, and by including the oft-neglected intermediate and minor axes. The structure of the paper is as follows. In § 2 we present the details of the simulation and describe the method used to measure the principal axes and angular momentum vectors of the halos. § 3 presents the overall shapes of the halos and how they change with radius. We discuss the internal alignment of the principal axes and angular momenta in § 4, while we explore the alignment of these quantities with external halos in § 5. We present a brief discussion of what these results imply for the origin of halo shapes and angular momenta in § 6, and summarize the results in § 7.

## 2. METHODOLOGY

### 2.1. *The simulation*

The simulation used here is the same as the one used in Bailin & Steinmetz (2004). It consists of  $512^3$   $N$ -body particles in a periodic box of length  $50 h^{-1}$  Mpc, in a low density flat universe ( $\Omega = 0.3$ ,  $\Omega_\Lambda = 0.7$ ,  $h = 0.7$ ,  $\sigma_8 = 0.9$ ). The particle mass is  $7.757 \times 10^7 h^{-1} M_\odot$ , and the force softening length is  $5 h^{-1}$  kpc. Halos were found using the standard friends-of-friends (FOF) algorithm with a linking length of 0.2 times the mean inter-particle separation.

In order to accurately measure the direction of the principal axes, many particles are needed. The direction of an axis can generally be determined to within an angle of

$$\theta_{\text{err}} = \frac{1}{2\sqrt{N}} \frac{\sqrt{r}}{1-r} \text{ radians}, \quad (2)$$

where  $N$  is the number of particles used and  $r$  is the relevant axis ratio:  $b/a$  for the major axis,  $c/b$  for the minor axis, and  $\max(b/a, c/b)$  for the intermediate axis (Bailin & Steinmetz 2004). For the purposes of measuring internal alignments, we would like the angular errors to be less than  $10^\circ$ . This requires on the order of 200 particles. Since each halo is split up into 6 radial shells, and

this accuracy is required in each shell, each halo should have over 1200 particles. For convenience, we adopt a cutoff of  $10^{11} h^{-1} M_{\odot}$  for the mass of the halo, or 1289 particles.

There are 3869 halos in the sample with masses extending from  $10^{11} h^{-1} M_{\odot}$  to  $2.8 \times 10^{14} h^{-1} M_{\odot}$ . 451 of the halos have masses in the range  $10^{12} - 10^{13} h^{-1} M_{\odot}$ , while 62 of the halos have masses greater than  $10^{13} h^{-1} M_{\odot}$ .

## 2.2. Measuring the axes

A standard technique to measure halo triaxiality in simulations is to use an iterative approach, where the particles are initially chosen to lie in a sphere or spherical shell, an ellipsoid is fit to these particles, and particles are chosen for the next iteration based on the new ellipsoid (e.g. W92). While this works for simulations that have sufficiently low resolution that overmerging erases substructure, we find in agreement with JS02 that in high resolution simulations, the presence of substructure prevents this technique from converging for a large fraction of halos.

JS02 have adopted a novel approach aimed at directly measuring isodensity contours. They assign SPH-like densities to halo particles, and then measure the principal axes and axis ratios of particles with densities near the nominal density of the isodensity contour. Due to the presence of substructure, this procedure often picks out disconnected shells in addition to the particles that define the isodensity contour of the smooth distribution. JS02 use the FOF algorithm to select the largest structure that fulfils the density criterion and therefore eliminate the substructure.

While this algorithm works well for very high-resolution halos, such as those JS02 use to demonstrate the technique (all of which contain  $N > 6 \times 10^5$  (Jing & Suto 2000)), we have run into difficulties using it on more moderate resolution halos. In particular, we find that it is not possible to find an optimal FOF linking length for eliminating substructure; if the linking length is too large, many “contours” contain obvious disconnected substructures, while reducing the linking length sufficiently to eliminate this problem reduces it to the point where in many halos, the single ellipsoid corresponding to the smooth distribution is broken up by the algorithm into several disconnected pieces. JS02’s algorithm also uses a relatively small number of particles to determine the shape. The error in the determination of the direction of the principal axes of a particle distribution goes as  $N^{-1/2}$  (see eq. [2]). Measuring the internal alignment of a halo requires small well-understood errors, and therefore as many particles as possible.

We take the following approach. The center of mass is calculated iteratively in spheres centred on the center of mass of the sphere in the previous iteration, starting with a sphere containing all of the particles. The radius of each successive sphere is reduced by 90%, and the procedure is iterated 25 times, by which point it has converged. The particles of each halo are transformed into this center of mass frame, and the velocities are transformed into the center of velocity frame. Each halo is then divided up into six concentric spherical shells with outer radii  $R$  of 1.0, 0.6, 0.4, 0.25, 0.12, and 0.06 times the virial radius  $r_{\text{vir}}$ . These radii are chosen to allow easy comparison to the isodensity contours of JS02. The

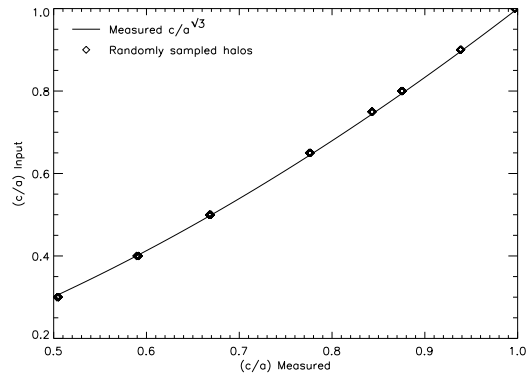


FIG. 1.— Measured versus input  $c/a$  axis ratio of randomly-sampled NFW and singular isothermal halos. At each input axis ratio, there are 12 independent points, representing the results for each of six radial bins and two different density profiles, but they are virtually indistinguishable. The solid line is the empirical fit of equation (4).

outer radius of each shell also forms the inner radius of the next larger shell, except for the innermost “shell”, which is actually a sphere extending to the halo center. One would like to use the inertia tensor to measure the principal axes of the mass distribution. However, the inertia tensor can be dominated by substructure in the outer part of the shell. Therefore, we weight particles by  $1/r^2$  so that each mass unit contributes equally regardless of radius (Gerhard 1983). Within each shell, we calculate this reduced moment of inertia tensor

$$\tilde{I}_{ij} = \sum_k \frac{r_{k,i} r_{k,j}}{r_k^2}, \quad (3)$$

which we then diagonalize. The axis ratios  $a$ ,  $b$ , and  $c$  are the square roots of the eigenvalues ( $a \geq b \geq c$ ), and the eigenvectors give the directions of the principal axes. There are no particles in common between radial shells, so the measurements of the axes at different radii are completely independent. We also calculate the angular momentum of the particles in each shell.

To calculate the error in the axis and angular momentum determinations, we perform a bootstrap analysis of the particles in each radial shell (Heyl, Hernquist, & Spergel 1994). If the shell contains  $N$  particles, we resample the shell by randomly selecting  $N$  particles from that set allowing for duplication and determine the axes and angular momentum from this bootstrap set. We do this 100 times for each radial shell. The dispersions of these estimates of the axis ratios, directions of the axes, magnitude of the angular momentum, and direction of the angular momentum around the measured values are taken formally as the “ $1\sigma$ ” error of each of these quantities.

Using spherical shells, rather than the ellipsoids defined by the isodensity contours as in JS02, does not affect the orientation of the principal axes. It does, however, bias the derived axis ratios toward spherical. To calibrate the magnitude of this bias, we have constructed prolate Poisson-sampled NFW (Navarro, Frenk, & White 1996) and singular isothermal halos with  $10^5$  particles each that have known  $c/a$  axis ratios ranging from 0.3 – 1. The NFW halos had concentration parameters  $c_{\text{vir}} = 10$ . In Figure 1 we plot

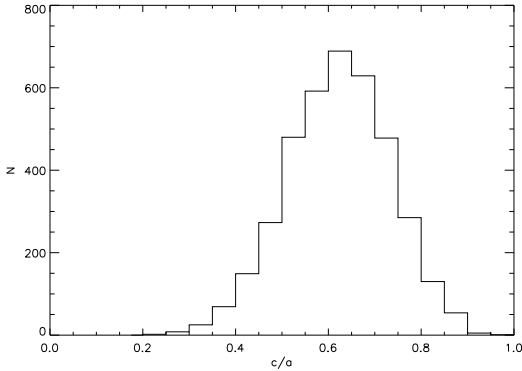


FIG. 2.— Histogram of the minor-to-major  $c/a$  axis ratio for each halo in the simulation, as measured in the  $R = 0.4 r_{\text{vir}}$  shell.

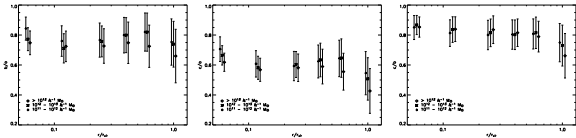


FIG. 3.— Median of the  $b/a$  (left),  $c/a$  (middle), and  $c/b$  (right) axis ratios for each radial shell. Crosses, asterisks, and diamonds represent the mass ranges  $10^{11} - 10^{12} h^{-1} M_{\odot}$ ,  $10^{12} - 10^{13} h^{-1} M_{\odot}$ , and  $10^{13} - 3 \times 10^{14} h^{-1} M_{\odot}$  respectively. Error bars represent the  $1\sigma$  width of the distribution. The error in the median is typically 0.002 for the crosses, 0.005 for the asterisks, and 0.01 for the diamonds. Crosses and diamonds are offset in radius for clarity.

the input  $c/a$  axis ratio for each combination of radial bin and density distribution as a function of the  $c/a$  ratio measured for the halos constructed using the method described above. The points for different radii and density distributions are virtually indistinguishable; the only important parameter is the input axis ratio. The solid line is an empirical fit to these points:

$$(c/a)_{\text{true}} = (c/a)_{\text{measured}}^{\sqrt{3}}. \quad (4)$$

The relationship for  $b/a$  is identical. The corrected axis ratios  $(b/a)_{\text{true}}$  and  $(c/a)_{\text{true}}$  are used throughout the remainder of this paper.

### 3. SHAPES

Dark matter halos are well approximated by ellipsoids (JS02) and are well described by the intermediate-to-major and minor-to-major axis ratios  $b/a$  and  $c/a$ . Figure 2 is a histogram of the  $c/a$  axis ratios as measured in the  $R = 0.4 r_{\text{vir}}$  shell for all of the halos in our sample. Unlike JS02, we find that they are not quite Gaussian, but rather have a tail toward very flattened halos as seen by KE04, although the tail is not as extreme as that seen by Bullock (2002). The distribution of  $b/a$  and  $c/a$  values measured at other radii have a similar shape. The lack of very flattened halos in JS02 may be a result of their exclusion of halos deemed to be interacting. The axis ratios we find are intermediate between the quite flattened halos found by JS02 and the more spherical halos found by KE04.

Early studies suggested that the coldness of the Sgr stream indicates that the dark matter halo of the Milky Way has  $c/a \gtrsim 0.8$  (Ibata et al. 2001; Majewski et al.

2003; Martínez-Delgado et al. 2004). Only 5% of the halos shown in Figure 2 have axis ratios so large. While this is not negligible, it is uncomfortably small, and forces us into the anti-Copernican situation of living in an exceptional galaxy. However, new models of the Sgr stream that are more careful about matching observations of the body of the dwarf find that the stars that constitute the stream were stripped from the body of the satellite too recently to have had time to undergo differential precession, thereby severely weakening the constraints on the halo ellipticity (Helmi 2004a,b). It should also be noted that our simulations do not take into account the effects of baryonic physics. There is some evidence that baryon cooling leads to more spherical halos (Dubinski 1994; Kazantzidis et al. 2004). Therefore systems in which most of the baryons have cooled, such as disk galaxies like the Milky Way, may have dark matter shapes that are more spherical than those presented here. Observations of external galaxies using a variety of methods find halo flattenings that range from 0.3 to 0.8, in agreement with our results (Sackett 1999).

The radial dependence of the axis ratios is shown in Figure 3. There are three distinct regions of the halo. Over most of the halo, the axis ratios increase with radius (i.e. the halos become more spherical). Near the virial radius, infalling unvirialized structure causes the axis ratios to drop. In the central 6% of the virial radius, the axis ratios rise. However, this is probably an artifact of the numerical softening (Bailin & Steinmetz 2004). Further evidence that this is a numerical effect comes from examining the location of this increase in sphericity for halos of different mass. The increase occurs at a larger fraction of the virial radius for low mass halos, i.e. at a similar physical radius. This complicated and non-monotonic radial dependence may explain the discrepancy between studies that have found that flattening increases with radius (Frenk et al. 1988; Cole & Lacey 1996; Bullock 2002) and those that have found that it decreases with radius (Dubinski & Carlberg 1991, W92, JS02). The mass dependence of the axis ratios is shown by the different symbols in Figure 3. The highest mass halos have smaller axis ratios at all radii than the smaller halos (W92; Bullock 2002; JS02; KE04). Our halos extend down to masses an order of magnitude smaller than any other study; the difference between the most massive halos (the diamonds) and the galaxy mass halos is more pronounced than the difference between different masses of galaxy halos. The high mass halos show particularly strong flattening near the virial radius.

As seen in Figure 3, the  $c/b$  ratio falls steadily with radius, indicating a transition from prolate figures in the center to oblate figures at large radii (Dubinski & Carlberg 1991; W92). Triaxiality can be quantified by the parameter  $T$ :

$$T = \frac{a^2 - b^2}{a^2 - c^2} \quad (5)$$

(Franx, Illingworth, & de Zeeuw 1991). Purely prolate halos have  $T = 1$  while purely oblate halos have  $T = 0$ . We have measured  $T$  at three radii:  $R = 1.0 r_{\text{vir}}$ , where infalling material results in substantial flattening,  $R = 0.6 r_{\text{vir}}$ , where the halos are at their least flattened, and  $R = 0.12 r_{\text{vir}}$ , where the interior of the halos are at their most flattened. Histograms of  $T$  at these

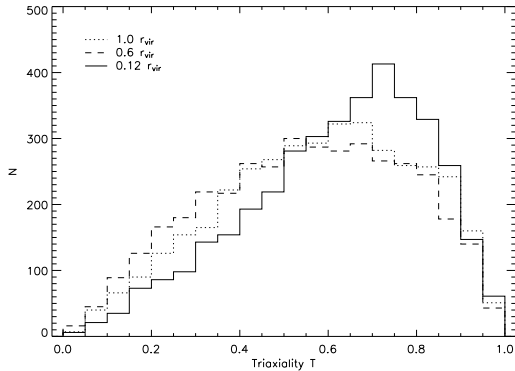


FIG. 4.— Histogram of the triaxiality  $T$  of all halos. The solid, dashed, and dotted histograms represent the halos measured at  $0.12$ ,  $0.6$ , and  $1.0$   $r_{\text{vir}}$  respectively.

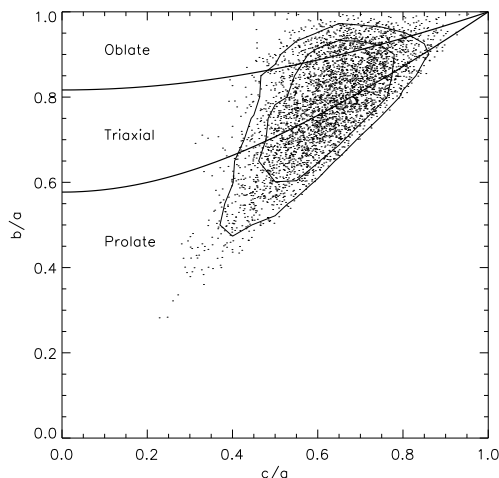


FIG. 5.— Intermediate axis ratio  $b/a$  as a function of minor axis ratio  $c/a$  for all of the halos, measured at  $R = 0.4 r_{\text{vir}}$ . The inner and outer contours enclose 68% and 90% of the halos respectively. The thick lines have constant values of the triaxiality parameter  $T$ . The separations between the prolate, triaxial, and oblate populations occur at  $T = 1/3$  and  $2/3$ .

radii are shown in Figure 4. The interior regions of halos clearly tend to be prolate (solid histogram). As the flattening decreases at larger radii, many of the halos become more oblate (dashed histogram), although still more are prolate than oblate. Near the virial radius, there is a small shift back toward prolate shapes (dotted histogram). Figure 5 shows the full relationship between  $b/a$  and  $c/a$  for all of the halos in our sample, measured at  $R = 0.4 r_{\text{vir}}$ , where the values are most typical for the halo as a whole. The preponderance of prolate and triaxial halos over oblate halos is clearly seen.

Weak lensing measurements have recently begun to probe the two-dimensional projected ellipticity of the lensing mass distribution (Hoekstra et al. 2004). For each halo in our sample, we have calculated the projected axis ratio  $q$  using the method of Stark (1977) for two random orientations, and calculated the ellipticity  $e$  using equation (1). A histogram of the results for the  $R = 0.4 r_{\text{vir}}$  shell is shown in Figure 6. The mean and median of the distribution of ellipticities are  $e_{\text{mean}} = 0.24$  and  $e_{\text{median}} = 0.23$  respectively, with a  $1\sigma$  width of 0.13.

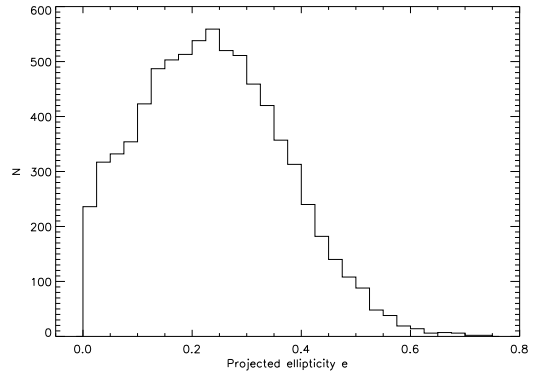


FIG. 6.— Projected ellipticity  $e$  of each halo seen from two random orientations, measured at  $R = 0.4 r_{\text{vir}}$ .

TABLE 1  
NUMBER OF HALOS WITH AXES DETERMINED TO WITHIN  
0.2 RADIANS

Radius ( $r_{\text{vir}}$ )	Major axis	Intermediate axis	Minor axis
0.06	904	388	621
0.12	2370	1005	1628
0.25	2942	1762	2540
0.4	2545	1488	2421
0.6	2322	1363	2324
1.0	2973	2231	2944

This is consistent with the lower limit of  $\langle e \rangle = 0.33^{+0.07}_{-0.09}$  found by Hoekstra et al. (2004) from stacked weak lensing measurements around galaxies. It is smaller than the ellipticities found by Croft & Metzler (2000) (note that they quantify ellipticity as  $e = (1 - q^2)/(1 + q^2)$ , in which units our mean ellipticity is  $e = 0.27$ ). However, most of the halos used in their study have higher masses than the galactic-mass halos studied here, and they included relatively poorly-resolved halos which may skew the results toward higher ellipticities.

## 4. INTERNAL ALIGNMENT

### 4.1. Principal axes

We compare the alignment of the principal axes within each halo to see whether the approximation of the halo as a set of concentric ellipsoids is justified (JS02). In order to determine whether the axes are aligned, the directions of the axes must be well determined, otherwise we may claim misalignments that are due to measurement error. Therefore, we restrict ourselves in this section to axes whose bootstrap error is less than 0.2 radians. The number of halos satisfying this criterion at each radius for each axis is given in Table 1.

To understand the effect of the error on the determination of the alignment, imagine two axes which are intrinsically perfectly aligned, but are each measured with an error of 0.2 radians (note that this is the worst possible case — the median error of the sample is 0.1 radians). Due to the measurement error, these axes will appear to be misaligned by an angle  $\theta_{\text{spurious}}$ . The component of an isotropic error in any particular plane, such as the

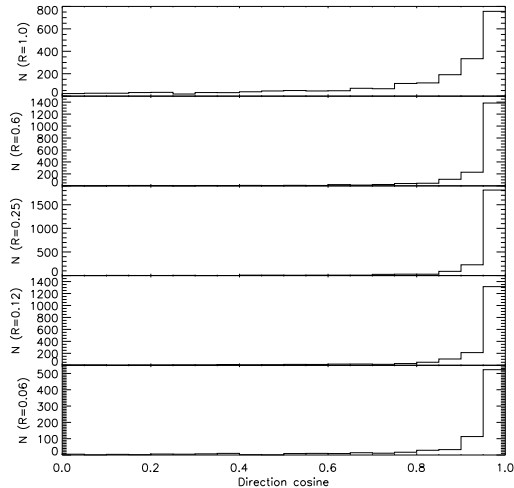


FIG. 7.— Histograms of the direction cosine between the major axis of the halo at  $R = 0.4 r_{\text{vir}}$  and the major axis at  $R = 1.0, 0.6, 0.25, 0.12,$  and  $0.06 r_{\text{vir}}$  (top to bottom). Due to the symmetry of the axes, this is always positive. Each histogram contains all halos where the major axes at both radii are determined to within 0.2 radians. If the axes were isotropic, this distribution would be uniform.

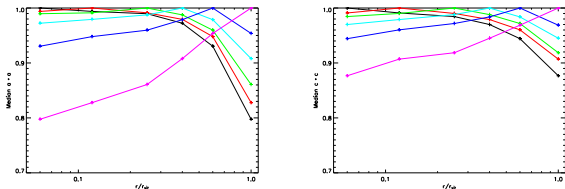


FIG. 8.— Median alignment of the major (*a-left*) and minor (*b-right*) axes at different radii. The alignment is with respect to the  $R = 0.06$  (black/solid),  $R = 0.12$  (red/dotted),  $R = 0.25$  (green/short-dashed),  $R = 0.4$  (cyan/dot-dashed),  $R = 0.6$  (blue/dot-dot-dot-dashed), and  $R = 1.0 r_{\text{vir}}$  (magenta/long-dashed) shell. For each pair of radii, only halos where the direction of the axis is determined to within 0.2 radians at both radii are used.

plane containing both of the measured axes, is half of the isotropic error, so we divide the isotropic error of 0.2 radians by two and add the error of each axis in quadrature to find the typical  $\theta_{\text{spurious}} \approx 0.14$ . Therefore, the cosine of the angle between the two axes, which is intrinsically 1.0, is measured to be  $\cos \theta_{\text{spurious}} = 0.990$ . If the axes are intrinsically perpendicular, in which case the effect of  $\theta_{\text{spurious}}$  on the direction cosine is maximized, the error in the direction cosine is 0.14. Most halos have well aligned axes (see below), so the error is negligible.

Figure 7 shows histograms of the alignment between the major axis of the  $R = 0.4 r_{\text{vir}}$  shell and the major axis of the outer (top two panels) and inner (bottom three panels) regions of the halo. The alignment is very good at all radii. The relative alignment of the major and minor axes as a function of radius is shown in Figure 8. Each line shows the median alignment with respect to a different fiducial radius, recognizable as the radius where the median is exactly unity. The axes are extremely well aligned within  $0.6 r_{\text{vir}}$ . Near the virial radius, some halos show deviations, but there is still usually very good

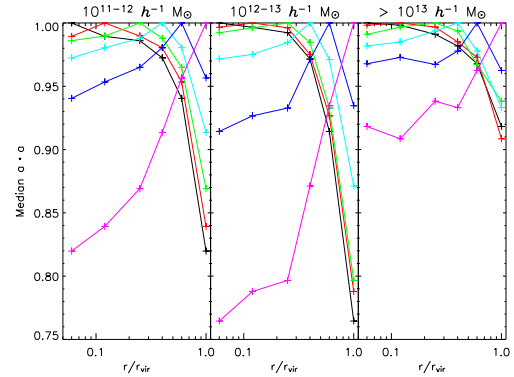


FIG. 9.— Median alignment of the major axis, as in Figure 8a, but only for halos with masses of  $10^{11} - 10^{12} h^{-1} M_{\odot}$  (*left*),  $10^{12} - 10^{13} h^{-1} M_{\odot}$  (*middle*), and  $10^{13} - 3 \times 10^{14} h^{-1} M_{\odot}$  (*right*). The alignment is with respect to the  $R = 0.06$  (black/solid),  $R = 0.12$  (red/dotted),  $R = 0.25$  (green/short-dashed),  $R = 0.4$  (cyan/dot-dashed),  $R = 0.6$  (blue/dot-dot-dot-dashed), and  $R = 1.0 r_{\text{vir}}$  (magenta/long-dashed) shell. For each pair of radii, only halos where the direction of the axis is determined to within 0.2 radians at both radii are used.

TABLE 2  
NUMBER OF  
HALOS WITH  
ANGULAR  
MOMENTUM  
DIRECTIONS  
DETERMINED TO  
WITHIN  
0.4 RADIANS

Radius	Halos
0.06	702
0.12	1686
0.25	2820
0.4	3060
0.6	3094
1.0	3229

alignment, especially for the minor axis. The alignment is better than that seen by JS02. This confirms their suggestion that many of the halos in which they measured poor alignment were nearly prolate or oblate. Such halos have large errors in their direction determination, and so are not included in our sample.

Figure 9 examines the internal alignment of the major axis as a function of halo mass. The inner  $0.4 r_{\text{vir}}$  of the halos are equally well aligned for halos of all masses. However, the outer half of the halo is better aligned with the rest of the halo in high mass halos than in low mass halos. JS02 saw a similar effect and suggested that it was because the low mass halos are intrinsically rounder and therefore have larger errors. We rule out this explanation, as halos with large errors are not included in our sample for any mass. Therefore, the better alignment within high mass halos appears to be a real physical effect.

#### 4.2. Angular momentum

The direction of the angular momentum cannot be determined as precisely as the direction of the principal axes. In order to have a reasonably large sample of ha-

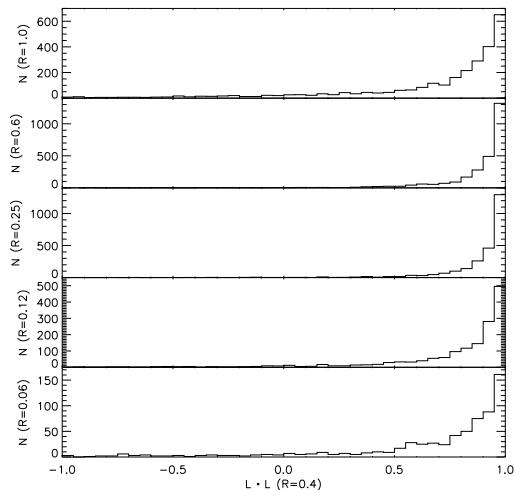


FIG. 10.— Histograms of the direction cosine between the angular momentum of the halo at  $R = 0.4 r_{\text{vir}}$  and the angular momentum at  $R = 1.0, 0.6, 0.25, 0.12,$  and  $0.06 r_{\text{vir}}$  (top to bottom). Each histogram contains halos whose angular momentum direction is determined to within 0.4 radians at both radii of the comparison. If the orientations were isotropic, this distribution would be uniform.

los, we use angular momentum vectors whose bootstrap error is less than 0.4 radians. This is twice as large as the limit adopted for the principal axis directions. The number of halos that satisfy this criterion at each radius is given in Table 2. Following the logic of § 4.1, the error in the direction cosine of two vectors with errors of 0.4 radians is 0.04 if they are perfectly aligned and 0.28 if they are perpendicular. The median errors of the samples are half of these worst-case scenarios. The alignment is shown to be good (see below), so the effect of the errors is negligible.

Figure 10 shows histograms of the relative alignment of the angular momentum of the  $R = 0.4 r_{\text{vir}}$  shell with the outer regions of the halo (upper two panels) and the inner regions of the halo (lower three panels). The alignment is very good at most radii.

The relative alignment of the angular momentum as a function of radius is shown in Figure 11. Each line shows the median alignment of the angular momentum with respect to a different fiducial radius, recognizable as the radius where the median is exactly unity. The alignment gets progressively worse as the radii get further separated; the median cosine between the angular momenta in the innermost and outermost regions is 0.64. However, the angular momentum vector at intermediate radius, such as at  $0.4 r_{\text{vir}}$ , is generally representative of its direction at all radii.

Figure 12 examines the internal alignment of the angular momentum as a function of halo mass. The patterns seen in Figure 11 generally hold for all masses, although the alignment between the very innermost and outermost regions is slightly worse for the highest mass halos.

#### 4.3. Alignment between the angular momentum and the halo shape

We investigate here the alignment between the angular momentum of a halo at a given radius and the principal

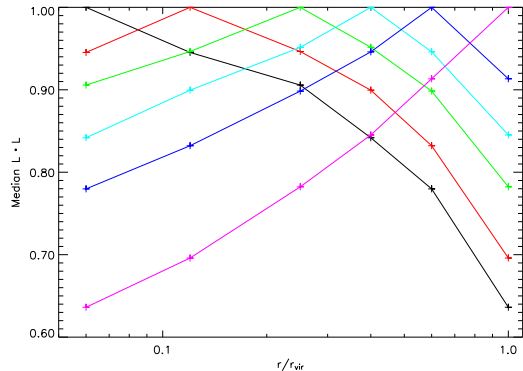


FIG. 11.— Median alignment of the angular momentum vector at different radii. The alignment is with respect to the  $R = 0.06$  (black/solid),  $R = 0.12$  (red/dotted),  $R = 0.25$  (green/short-dashed),  $R = 0.4$  (cyan/dot-dashed),  $R = 0.6$  (blue/dot-dot-dashed), and  $R = 1.0 r_{\text{vir}}$  (magenta/long-dashed) shell. For each pair of radii, only halos where the direction of the angular momentum vector is determined to within 0.4 radians at both radii are used.

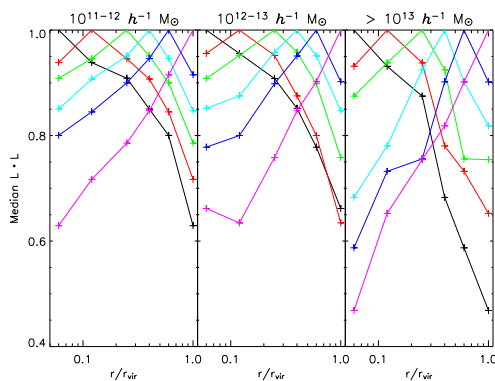


FIG. 12.— Median angular momentum alignment as in Figure 11, but only for halos with masses of  $10^{11} - 10^{12} h^{-1} M_{\odot}$  (left),  $10^{12} - 10^{13} h^{-1} M_{\odot}$  (middle), and  $10^{13} - 3 \times 10^{14} h^{-1} M_{\odot}$  (right). The alignment is with respect to the  $R = 0.06$  (black/solid),  $R = 0.12$  (red/dotted),  $R = 0.25$  (green/short-dashed),  $R = 0.4$  (cyan/dot-dashed),  $R = 0.6$  (blue/dot-dot-dashed), and  $R = 1.0 r_{\text{vir}}$  (magenta/long-dashed) shell. For each pair of radii, only halos where the direction of the angular momentum vector is determined to within 0.4 radians at both radii are used.

axes of the mass distribution at that radius. If we compare an angular momentum vector whose error is 0.4 radians with a principal axis whose error is 0.2 radians, the error in the direction cosine is 0.02 if they are perfectly aligned and 0.22 if they are perpendicular. The median errors are half of those values. Therefore, in the cases where the alignment is good, the effect of the errors is negligible. In the cases where the vectors are perpendicular or isotropic, we must take the errors into account when drawing conclusions.

Figures 13, 14, and 15 show histograms of the cosine between the direction of the angular momentum vector and the major, intermediate, and minor axis respectively. Only those halos with both angular momentum direction errors of less than 0.4 radians and axis direction errors of less than 0.2 radians are used. The angular momentum vector tends to be perpendicular to the major and intermediate axes, and parallel with the minor axis. Because

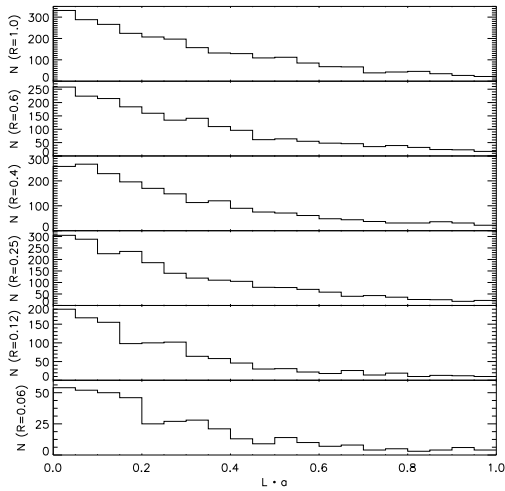


FIG. 13.— Histograms of the alignment between the angular momentum vector and the major axis of the  $R = 1.0, 0.6, 0.4, 0.25, 0.12,$  and  $0.06 r_{\text{vir}}$  (top to bottom) shell of each halo where the error in the major axis direction is less than  $0.2$  radians and the error in the angular momentum direction is less than  $0.4$  radians at that radius. Due to the symmetry of the axes, the direction cosine is always positive. If the orientations were random, this distribution would be uniform.

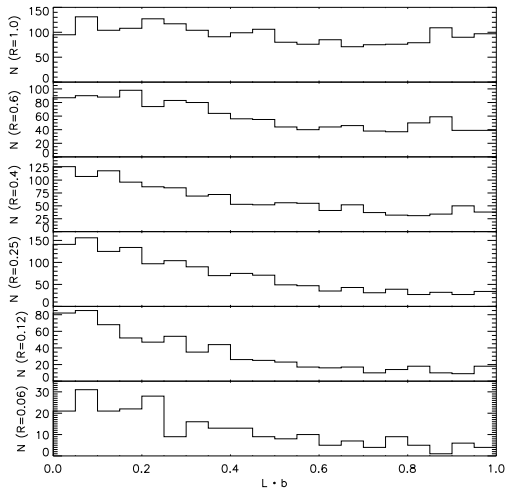


FIG. 14.— As in Figure 13 but for the intermediate axis.

of the different effects of the error on parallel and perpendicular vectors, the tendency of the angular momentum to be perpendicular to the major axis is as significant as the trend for it to be parallel to the minor axis, despite the different appearance of the histograms. The angular momentum tends to lie perpendicular to the intermediate axis, but this trend gets weaker with radius.

These results are consistent with those of Barnes & Efstathiou (1987), Dubinski (1992), and W92. Of these, only W92 quantify any change with radius; they found slightly better alignment at larger radii, in contrast to the results presented here. However,

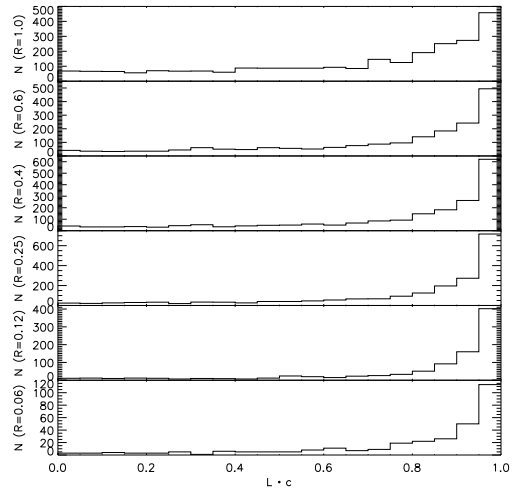


FIG. 15.— As in Figures 13 and 14 but for the minor axis.

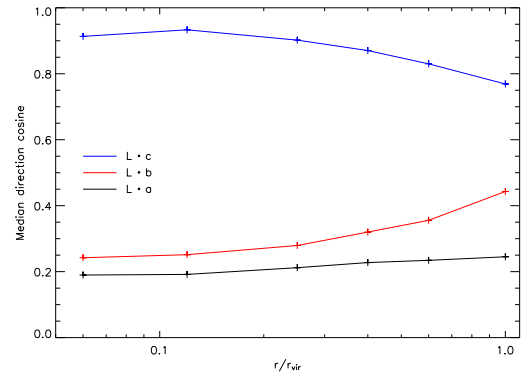


FIG. 16.— Median alignment between the angular momentum vector and the major (black/solid), intermediate (red/dotted), and minor (blue/dashed) axis of each halo as a function of radius within the halo.

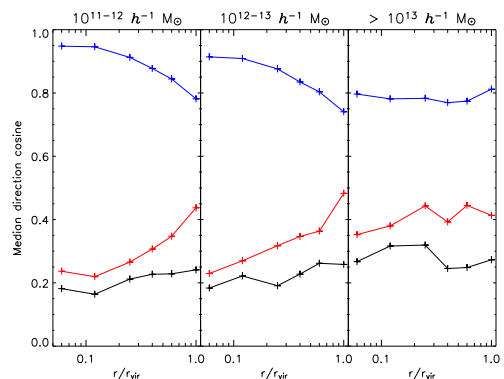


FIG. 17.— As in Figure 16, but only for halos with masses of  $10^{11} - 10^{12} h^{-1} M_{\odot}$  (left),  $10^{12} - 10^{13} h^{-1} M_{\odot}$  (middle), and  $10^{13} - 3 \times 10^{14} h^{-1} M_{\odot}$  (right).

both of the radii at which they performed the comparison were well within the virial radius, well inside the radii where we see the alignment drop.

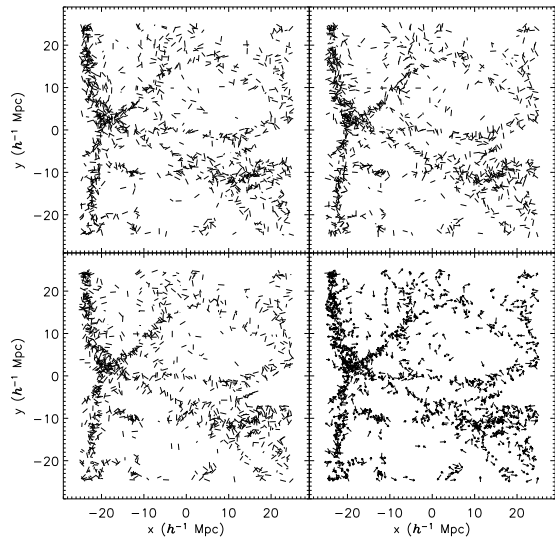


FIG. 18.— Projection in  $xy$  of the major (*top-left*), intermediate (*top-right*), and minor (*bottom-left*) axes, and unit angular momentum vectors (*bottom-right*) of halos in a slab of depth  $\Delta z = 12.5 h^{-1} \text{ Mpc}$  (one quarter of the simulation volume). The three-dimensional length of each line or vector is  $1.5 h^{-1} \text{ Mpc}$ , including the unseen  $z$  component.

These relationships are summarized in Figure 16, which shows the median alignment between the angular momentum vector and each of the principal axes. The angular momentum tends to lie parallel with the minor axis and perpendicular to both the major and intermediate axes. These trends are strongest in the central  $0.25 r_{\text{vir}}$  of the halo, deteriorating slightly in the outer regions. Figure 17 shows how these trends depend on the halo mass. For high mass halos, the alignment is slightly worse and has less of a dependence on the location within the halo.

## 5. EXTERNAL ALIGNMENT

### 5.1. Introduction

In this section, we compare the orientation of the principal axes and angular momenta of individual halos with the location of mass around them and the orientation of those properties in surrounding halos. For each halo, the volume is split into 7 radial bins. The nearest bin spans separations from 0 to  $390.625 h^{-1} \text{ kpc}$ . The outer radii double for each subsequent bin, while the inner radius is equal to the outer radius of the interior bin. The largest bin has an outer radius of  $25 h^{-1} \text{ Mpc}$ , extending to the edge of the periodic box. The properties of the halos in the  $R = 0.4 r_{\text{vir}}$  shell are characteristic of their overall properties over a large range of radii (see § 4). Therefore, we use the principal axes and angular momenta measured at this radius for all halos in this section.

We follow the nomenclature of Splinter et al. (1997), and use “alignment” to refer to the tendency of a vector (such as a principal axis or an angular momentum vector) to point toward or away from other halos, and “correlation” to refer to the tendency of vectors in different halos to point in the same direction.

A visual impression of how the axes and angular momenta align can be seen in Figure 18, which shows the axes and angular momentum vectors of all of the ha-

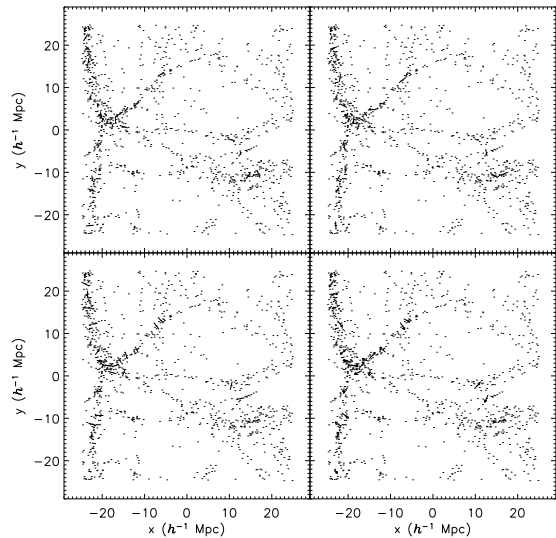


FIG. 19.— As in Figure 18, but for only those halos with masses greater than  $10^{13} h^{-1} M_{\odot}$ . The three-dimensional length of each line or vector is  $2 h^{-1} \text{ Mpc}$ , including the unseen  $z$  component. Dots show the positions of all halos, regardless of mass.

los in a slab containing one quarter of the simulation. If the axis or vector lies mostly in the  $z$  direction, it appears much shorter in the  $xy$  projection shown. Figure 19 shows the properties of only the high mass halos,  $M > 10^{13} h^{-1} M_{\odot}$ , with the location of the other halos shown as dots. Because of the filamentary nature of the large scale structure (e.g. Colberg et al. 1999), positive alignment indicates that a quantity tends to point along filaments.

### 5.2. Axis alignments

We compare here the alignment of the principal axes of the halos with the location of surrounding structure. Methods of measuring these alignments vary in the literature, as does the nomenclature for a given metric. We adopt an internally-consistent nomenclature  $\xi_{xy}$  and  $\xi_{|xy|}$ , which are defined to be the mean value of the direction cosine between direction  $x$  and direction  $y$ , and the mean of the absolute value of the direction cosine respectively. We note names other authors use for the same quantities when applicable. For example, to measure the alignment of the major axis, whose direction is defined by the unit vector  $\hat{\mathbf{a}}$ , with the large scale structure, we calculate the alignment  $\xi_{|ar|}$ :

$$\xi_{|ar|}(r) \equiv \langle |\hat{\mathbf{a}} \cdot \hat{\mathbf{r}}| \rangle \equiv \frac{1}{N} \sum_{i,j} |\hat{\mathbf{a}}_i \cdot \hat{\mathbf{r}}_{ij}|, \quad (6)$$

where the sum over  $i$  is over all halos in the primary sample, the sum over  $j$  is over all halos in the secondary sample,  $\hat{\mathbf{r}}_{ij}$  is a unit vector in the direction of the displacement from halo  $i$  to halo  $j$ , and  $N$  is the number of terms in the double sum. The primary sample consists of all halos whose major axis is determined to within 0.2 radians, while the secondary sample consists of all halos. We define the alignments  $\xi_{|br|}$  and  $\xi_{|cr|}$  for the intermediate axis  $\hat{\mathbf{b}}$  and the minor axis  $\hat{\mathbf{c}}$  similarly. Note that the primary samples used to define  $\xi_{|ar|}$ ,  $\xi_{|br|}$ , and  $\xi_{|cr|}$  are

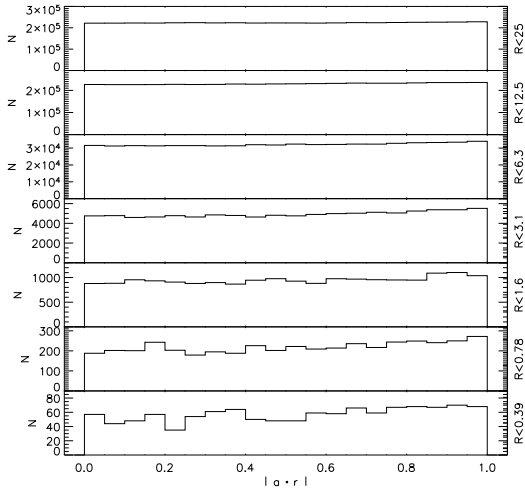


FIG. 20.— Histograms of the direction cosine  $|\hat{\mathbf{a}} \cdot \hat{\mathbf{r}}|$  between the major axes of halos in the primary sample and the displacement from each primary halo to all surrounding halos, binned by radial separation between the centers of the halos. The direction cosine is always positive due to the symmetry of the axes. If the axes were randomly oriented, the distributions would be uniform. The radial bins consist of halos separated by (top to bottom): 12.5 – 25, 6.25 – 12.5, 3.125 – 6.25, 1.5625 – 3.125, 0.78125 – 1.5625, 0.390625 – 0.78125, and 0 – 0.390625  $h^{-1}$  Mpc respectively. The primary sample consists of halos whose major axes are determined to within 0.2 radians.

not identical, as the set of halos with good major axis determinations is deficient in very oblate halos, the set of halos with good minor axis determinations is deficient in very prolate halos, and the set of halos with good intermediate axis determinations is deficient in both very prolate and very oblate halos.

Figure 20 shows histograms of the distribution of direction cosines  $|\hat{\mathbf{a}} \cdot \hat{\mathbf{r}}|$  for halos at a variety of separations. If the axes were randomly oriented, the distributions would be uniform. If  $|\hat{\mathbf{a}} \cdot \hat{\mathbf{r}}| > 0.5$  then the axes tend to be parallel to the lines connecting halos, while if  $|\hat{\mathbf{a}} \cdot \hat{\mathbf{r}}| < 0.5$  then the axes tend to point perpendicular to the lines connecting halos. The distribution is mostly isotropic, but there is an excess of halos with  $|\hat{\mathbf{a}} \cdot \hat{\mathbf{r}}| > 0.5$ . We quantify this by calculating the mean,  $\xi_{|ar|}$  (note that this is similar but not identical to the quantity  $w(r)$  used by KE04).

Figure 21 shows  $\xi_{|ar|}$  for the halos. Each bin is plotted at the geometric mean between its inner and outer radius, except for the innermost bin which is plotted at  $1/\sqrt{2}$  times its outer radius. The inner bin has no formal inner radius, but in practice is limited by twice the radial extent of the typical halo, or 250  $h^{-1}$  kpc. Halos whose centers of mass are closer to each other than this are merging, and are detected as a single object by the group finder. We find that the alignments are usually well fit by a power law over a wide range of separations. The fit is shown as the solid line in Figure 21, and is given by

$$\xi_{|ar|}(r) = \frac{1}{2} + m_1 r^\alpha, \quad (7)$$

where  $r$  is the separation in units of  $h^{-1}$  Mpc, the alignment at 1  $h^{-1}$  Mpc is  $m_1 = 0.015$ , and the slope is

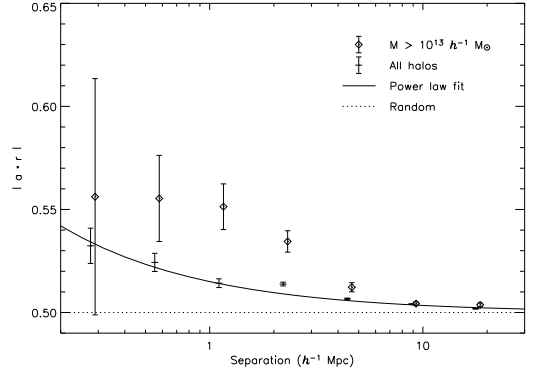


FIG. 21.— Mean alignment  $\xi_{|ar|}$  between the major axes of halos in the primary sample and the displacement from the primary halos to all surrounding halos. This is the tendency for the major axes to point along filaments. Only halos where the major axis is determined to within 0.2 radians are used for the primary sample. The different symbols are for primary samples consisting of all such halos (crosses) or of only those with masses greater than  $10^{13} h^{-1} M_\odot$  (diamonds). The diamonds are shifted slightly to the right for clarity. The values are binned by radial separation between the centers of the halos. The ordinate for each bin is the outer radius of the bin divided by  $\sqrt{2}$ , which is the geometric mean radius of the bin for all but the central bin, which nominally extends to zero radius but in practice is limited by twice the radial extent of the halos, or typically  $\sim 250 h^{-1}$  kpc in our sample. Error bars represent the  $1\sigma$  Poisson sampling error in the mean. Values greater than 0.5 indicate that the axes lie parallel to the filaments, while values less than 0.5 indicate that the axes lie perpendicular to the filaments. The solid line is the power law fit for the full sample given by equation (7). The dotted line is the value expected for random orientations.

$\alpha = -0.64$ . F02 find even stronger alignment for their cluster-mass halos, as do KE04 (except at the very smallest separations, which is at the spatial limit of their simulations). To see whether the halo mass is important, we recalculate  $\xi_{|ar|}$ , restricting the primary sample to those halos with masses greater than  $10^{13} h^{-1} M_\odot$ . This is the tendency for the major axes of group or cluster mass halos to point along the filaments. The results are shown as the diamonds in Figure 21. The group and cluster mass halos are much more strongly aligned than the full sample (which is dominated by galaxy mass halos). The alignment  $\xi_{|ar|}$  is constant out to 3  $h^{-1}$  Mpc, after which it drops until it agrees with the results of the full sample by 6  $h^{-1}$  Mpc. The orientation of clusters is influenced in large part by the accretion of substructure (van Haarlem & van de Weygaert 1993). The substructure is accreted along filaments, and therefore groups and clusters tend to be strongly aligned with surrounding halos to larger radii. KE04 find stronger alignments out to even larger separations. Their simulations are performed in a much larger (Hubble volume) box, which contains power on longer wavelengths than exist in our smaller simulation volume (and allows them to measure alignments at separations far exceeding our entire box length). Alternatively, it may be a consequence of the higher mass of their halos; while there is virtually no overlap in the range of halo masses between this work and KE04, we find that the alignment is a strong function of halo mass. As KE04 do not present independent results for their lowest mass halos (which are the closest match to our “high mass halo” sample), we cannot tell

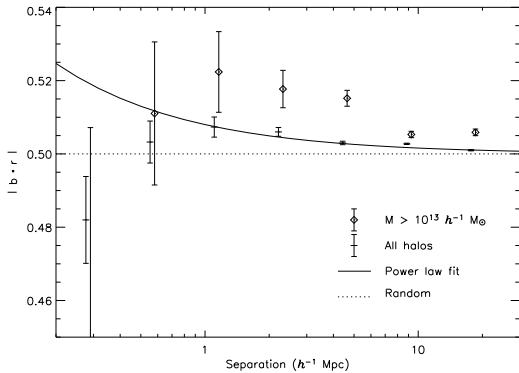


FIG. 22.— As in Figure 21, but for the intermediate axis,  $\xi_{|br|}$ . The solid line is the power law fit for the outer 5 points of the full sample, i.e. for  $r > 781 h^{-1}$  kpc, and is given by equation (8).

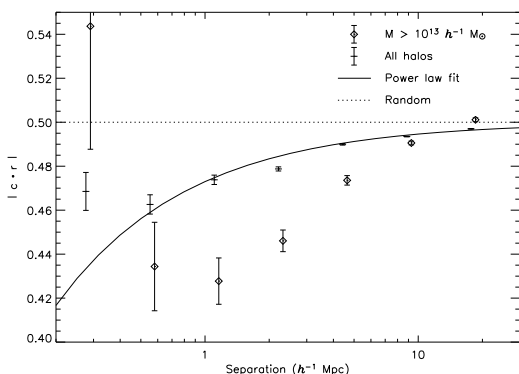


FIG. 23.— As in Figures 21 and 22, but for the minor axis,  $\xi_{|cr|}$ . The solid line is the power law fit for the full sample, excluding the innermost bin, i.e. for  $r > 391 h^{-1}$  kpc, and is given by equation (9).

which of these factors dominates the difference between the results.

The intermediate axes are also aligned with the filaments. The mean alignment as a function of radius is shown in Figure 22. While the innermost bins show no alignment, there is clear evidence of alignment at separations of  $1 h^{-1}$  Mpc and beyond. The solid line is a power law fit to the outer 5 points, i.e. for  $r > 781 h^{-1}$  kpc, and is given by

$$\xi_{|br|} = \frac{1}{2} + m_1 r^\alpha, \quad (8)$$

where  $m_1 = 0.008$  and  $\alpha = -0.7$ . The high mass halos again show constant alignment out to several Mpc.

As both the major and intermediate axes tend to point along filaments, the minor axis must tend to lie perpendicular to the filaments. This trend can be clearly seen in the bottom-left panels of Figures 18 and 19 as sequences of parallel lines running along the filaments. Figure 23 shows  $\xi_{|cr|}$ . The solid line is a power law fit for the full sample excluding the innermost bin, i.e. for  $r > 391 h^{-1}$  kpc, and is given by

$$\xi_{|cr|}(r) = \frac{1}{2} - m_1 r^\alpha, \quad (9)$$

where the alignment at  $1 h^{-1}$  Mpc is  $m_1 = 0.027$  and  $\alpha = -0.7$ . The minor axes of group and cluster mass halos

show even stronger alignment, as seen by the diamonds in Figure 23.

The relative strength of the alignment for the different axes is well described by  $m_1$ , the value of the power law fit at a separation of  $1 h^{-1}$  Mpc. This is 0.015, 0.008, and 0.027 for the major, intermediate, and minor axes respectively. Therefore it is the minor axis, not the major axis, that is most influenced by the presence of surrounding material. This also explains how both the major and intermediate axes can be positively aligned with the filament: if the minor axis of a halo lies perpendicular to the filament, then both the major and intermediate axes are constrained to lie within a plane that contains the filament. Therefore, they are both more likely to point along the filament than a randomly-oriented three-dimensional axis, and therefore both show positive alignment (for example, if all of the minor axes were perfectly perpendicular to the filament and there were no difference between the major and intermediate axes, then  $\xi_{|cr|}$  would vanish and both  $\xi_{|ar|}$  and  $\xi_{|br|}$  would equal  $2/\pi \approx 0.64$ ). The geometry of the environment is not strictly linear, especially at larger scales. However, despite these complications, the relationships we have found provide useful quantitative predictions that can be tested when full three-dimensional observations of halo shapes are available.

### 5.3. Axis correlations

We compare here the tendency for the principal axes of neighbouring halos to point in the same direction. The procedure we use is completely analogous to that used to calculate the alignments in § 5.2. The correlation between the major axes is defined as

$$\xi_{|aa|}(r) \equiv \langle |\hat{\mathbf{a}}_i \cdot \hat{\mathbf{a}}_j| \rangle \equiv \frac{1}{N} \sum_{i,j} |\hat{\mathbf{a}}_i \cdot \hat{\mathbf{a}}_j|, \quad (10)$$

where the sum is over all unique pairs  $(i, j)$  because the measurement is symmetric with respect to each pair of halos. If the major axes lie parallel to each other,  $|\hat{\mathbf{a}}_i \cdot \hat{\mathbf{a}}_j| > 0.5$ , while if they lie perpendicular to each other,  $|\hat{\mathbf{a}}_i \cdot \hat{\mathbf{a}}_j| < 0.5$ . Only halos whose major axes are determined to within 0.2 radians are used for both the primary and secondary sample.

Figure 24 plots the mean correlation  $\xi_{|aa|}$  of the major axes as a function of the halo separation (this is identical to the quantity defined as  $u(r)$  in KE04). Although almost all bins are individually consistent with isotropy, they all lie above 0.5, and taken together are evidence that the directions of the major axes are correlated. We fit a power law and find

$$\xi_{|aa|}(r) = \frac{1}{2} + m_1 r^\alpha, \quad (11)$$

where  $r$  is the separation in units of  $h^{-1}$  Mpc, the correlation at  $1 h^{-1}$  Mpc is  $m_1 = 0.004$ , and the slope is  $\alpha = -1.2$ , although the large errors introduce considerable uncertainties in these values. The correlations found by both F02 and KE04 are considerably stronger than those found here. We have recalculated  $\xi_{|aa|}$  using only halos with masses greater than  $10^{13} h^{-1} M_\odot$  to see if the behaviour of high mass halos differs from those of lower mass, but due to the small number of halos in our sample in this mass range, the errors are too large draw any conclusions.

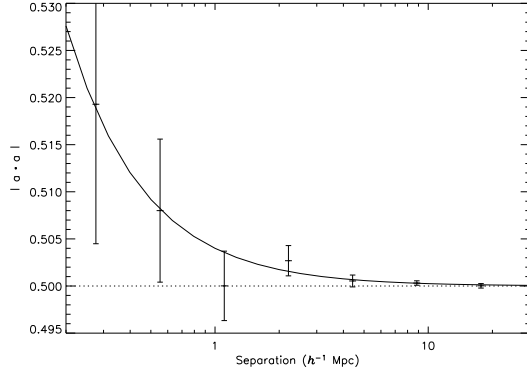


FIG. 24.— Mean correlation  $\xi_{|aa|}$  of the major axes of halos for which the direction of the major axes is determined to within 0.2 radians for both halos. The solid line is the power law fit, and is given by equation (11). The dotted line is the expected value for random orientations. Error bars represent the  $1\sigma$  Poisson sampling error in the mean. Values greater than 0.5 indicate that the major axes are parallel to each other, while values less than 0.5 indicate that the axes are perpendicular to each other.

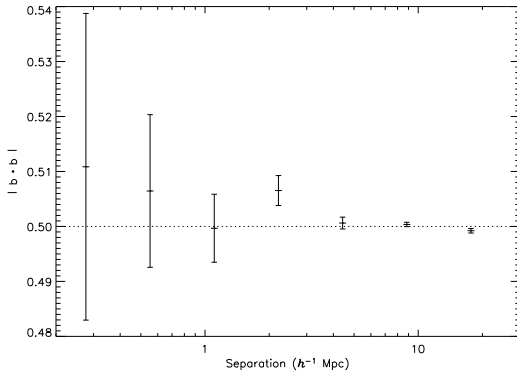


FIG. 25.— As in Figure 24, but for the intermediate axis,  $\xi_{|bb|}$ .

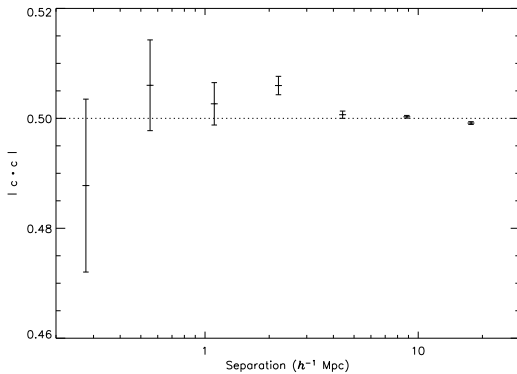


FIG. 26.— As in Figures 24 and 25, but for the minor axis,  $\xi_{|cc|}$ .

In Figures 25 and 26, we plot the mean correlations of the intermediate and minor axes of the halos,  $\xi_{|bb|}$  and  $\xi_{|cc|}$ . The error bars are too large to robustly detect any correlation, though the preponderance of bins in Figure 26 with  $\xi_{|cc|} > 0.5$  is suggestive. A larger sample of halos simulated at equally high spatial resolution is required to see if this is real.

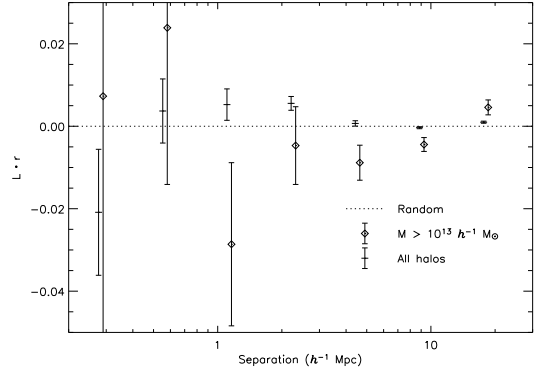


FIG. 27.— Mean alignment  $\xi_{Lr}$  between the angular momentum vector of a halo and the location of surrounding halos, as a function of radial separation. Only halos where the direction of the angular momentum is determined to within 0.4 radians are used for the primary samples. The different symbols are for primary samples consisting of all such halos (crosses), or of only those with masses greater than  $10^{13} h^{-1} M_{\odot}$  (diamonds). The diamonds are shifted slightly to the right for clarity. Error bars represent the  $1\sigma$  Poisson sampling error in the mean. Positive values indicate that the angular momentum tends to point toward local density enhancements, while negative values indicate that the angular momentum points away from them. The dotted line is the expected value for random orientations.

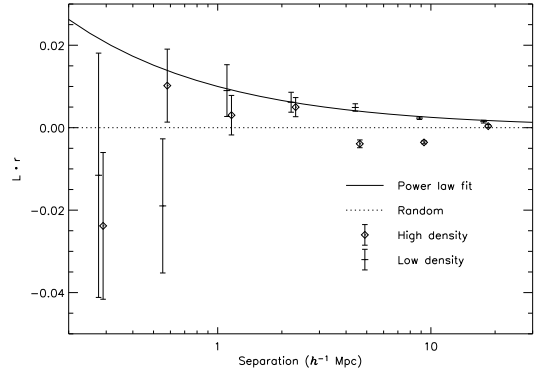


FIG. 28.— Mean alignment  $\xi_{Lr}$  as in Figure 27, with primary samples selected by local density. Crosses designate halos that have 3 or fewer neighbouring halos within  $2 h^{-1}$  Mpc, while diamonds designate halos with 4 or more neighbouring halos within  $2 h^{-1}$  Mpc. The solid line is the power law fit for the low density sample at  $r > 781 h^{-1}$  kpc, and is given by equation (13).

#### 5.4. Angular momentum

We investigate the tendency for the angular momentum to point toward or away from nearby halos, for it to lie parallel or perpendicular to the filamentary structure, and for the angular momentum vectors of neighbouring halos to point in the same direction. To measure the tendency of halo angular momenta to point toward or away from other halos, we calculate the alignment

$$\xi_{Lr}(r) \equiv \langle \hat{\mathbf{L}} \cdot \hat{\mathbf{r}} \rangle \equiv \frac{1}{N} \sum_{i,j} \hat{\mathbf{L}}_i \cdot \hat{\mathbf{r}}_{ij}, \quad (12)$$

where  $\hat{\mathbf{L}}_i$  is a unit vector in the direction of the angular momentum vector for halo  $i$ , and  $\hat{\mathbf{r}}_{ij}$  is a unit vector in the direction of the displacement from halo  $i$  in the primary sample to halo  $j$  in the secondary sample. The primary sample consists of all halos where the direction

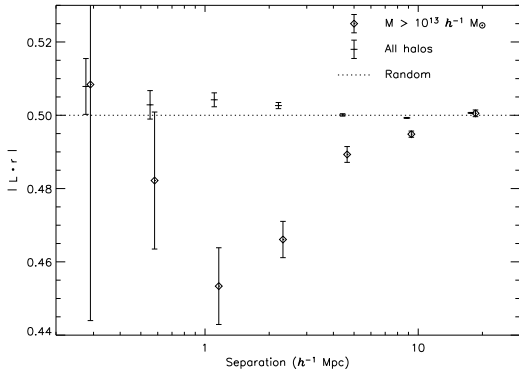


FIG. 29.— Mean alignment  $\xi_{|Lr|}$  between the angular momentum vector of primary halos and the location of all surrounding halos. Only halos where the direction of the angular momentum is determined to within 0.4 radians are used for the primary samples. The different symbols are for primary samples consisting of all such halos (crosses), or of only those with masses greater than  $10^{13} h^{-1} M_{\odot}$  (diamonds). The diamonds are shifted slightly to the right for clarity. Error bars represent the  $1\sigma$  Poisson sampling error in the mean. Values greater than 0.5 indicate that the angular momentum vectors point parallel to the filaments, while values less than 0.5 indicate that the angular momentum vectors point perpendicular to the filaments. The dotted line is the expected value for random orientations.

of the angular momentum is determined to within 0.4 radians, while the secondary sample consists of all halos. Figure 27 shows the results. There may be a weak tendency for the angular momentum to point toward local density enhancements on scales of  $0.5 - 3 h^{-1}$  Mpc, but the size of the error bars makes such a result tentative. The high mass halos show no alignment.

Kashikawa & Okamura (1992) and Navarro et al. (2004) have found that galaxies within the local supercluster have their spins pointing within the supercluster plane, while those at least  $2 h^{-1}$  Mpc from the plane have spins that point toward or away from the plane. To see if the behaviour of simulated halos in low and high density regions differs, we have split the sample into those halos that have 3 or fewer neighbouring halos within  $2 h^{-1}$  Mpc (the low density sample), and those that have 4 or more neighbours within  $2 h^{-1}$  Mpc (the high density sample). There are 2155 and 1714 halos in the low and high density samples respectively. In Figure 28, we have plotted the alignment  $\xi_{Lr}$  against separation for the two samples. By construction, there are very few pairs (and therefore large error bars) at small separations in the low density sample, but beyond  $1 h^{-1}$  Mpc there is a clear detection of positive alignment in this sample. The alignment is well fit by a power law of the form

$$\xi_{Lr} = m_1 r^\alpha, \quad (13)$$

where  $r$  is the separation in units of  $h^{-1}$  Mpc, the correlation at  $1 h^{-1}$  Mpc is  $m_1 = 0.01$ , and the slope is  $\alpha = -0.6$ . The high density sample shows no coherent tendency for the angular momentum vectors to point toward or away from density enhancements. The low and high density samples do not show significant deviations from the full sample for any of the other statistics studied.

The tendency for the angular momentum vectors to lie parallel versus perpendicular to the filaments is measured

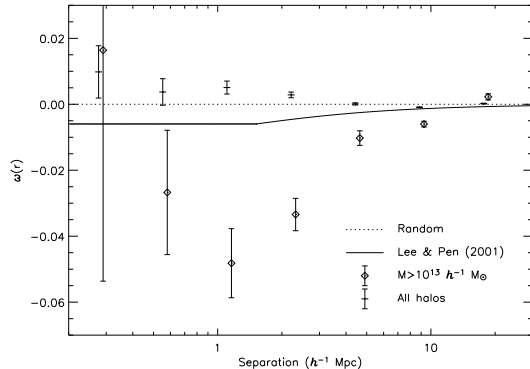


FIG. 30.— Alignment  $\omega(r)$  between the angular momentum vector of a primary halo and the location of all surrounding halos. Only halos where the direction of the angular momentum is determined to within 0.4 radians are used for the primary samples. The different symbols are for primary samples consisting of all such halos (crosses), or of only those with masses greater than  $10^{13} h^{-1} M_{\odot}$  (diamonds). The diamonds are shifted slightly to the right for clarity. Error bars represent the  $1\sigma$  Poisson sampling error. Positive values indicate that the angular momentum vectors tend to point parallel to the filaments, while negative values indicate that the angular momentum vectors point perpendicular to the filaments. The dotted line is the expected value for random orientations, while the solid line is the prediction from linear tidal torque theory (Lee & Pen 2001).

by

$$\xi_{|Lr|}(r) \equiv \left\langle |\hat{\mathbf{L}} \cdot \hat{\mathbf{r}}| \right\rangle \equiv \frac{1}{N} \sum_{i,j} |\hat{\mathbf{L}}_i \cdot \hat{\mathbf{r}}_{ij}|, \quad (14)$$

defined as  $L_{||}$  in Hatton & Ninin (2001), or

$$\omega(r) \equiv \left\langle |\hat{\mathbf{L}} \cdot \hat{\mathbf{r}}|^2 \right\rangle - \frac{1}{3} \equiv \frac{1}{N} \sum_{i,j} |\hat{\mathbf{L}}_i \cdot \hat{\mathbf{r}}_{ij}|^2 - \frac{1}{3}, \quad (15)$$

as used by Lee & Pen (2001). If  $\xi_{|Lr|} > 0.5$  or  $\omega(r) > 0$  then the angular momentum vectors lie parallel to the filaments, while if  $\xi_{|Lr|} < 0.5$  or  $\omega(r) < 0$  then the angular momentum vectors point perpendicular to the filaments. In Figures 29 and 30, we plot  $\xi_{|Lr|}$  and  $\omega(r)$  respectively. The solid line in Figure 30 shows the prediction of Lee & Pen (2001) from linear tidal torque theory. On scales less than  $3 h^{-1}$  Mpc, the angular momentum tends to lie parallel to the filaments. The values are consistent with those found by Hatton & Ninin (2001). However, both Lee & Pen (2001) and F02 find that the angular momenta of halos tend to lie perpendicular to the filaments. This discrepancy may lie in the different mass ranges probed. The halos of Hatton & Ninin (2001) cover a very similar mass range to those in this work, while the sample of F02 consists entirely of cluster mass halos (their *smallest* halo has a mass of  $1.4 \times 10^{14} h^{-1} M_{\odot}$ , nearly the mass of our *largest* halo). We have recalculated  $\xi_{|Lr|}$  and  $\omega(r)$  using only halos with masses greater than  $10^{13} h^{-1} M_{\odot}$  in the primary sample and plotted them as diamonds in Figures 29 and 30. The behaviour is radically different; the angular momenta of groups and clusters tend to point perpendicular to the filaments.

The correlations between the angular momentum vectors of halos are calculated analogously. In particular, the tendency for halo angular momenta to point in the same direction versus in the opposite direction as the

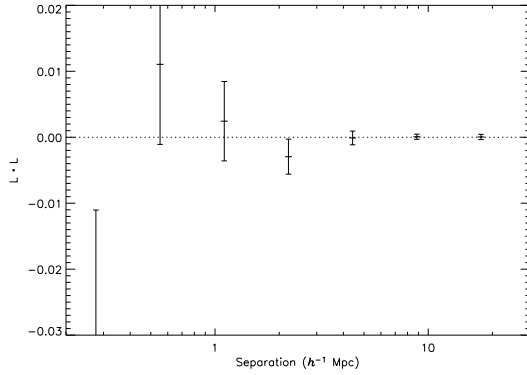


FIG. 31.— Mean correlation  $\xi_{LL}$  of the angular momentum vectors of halos as a function of their separation. All halos where the direction of the angular momentum is determined to within 0.4 radians are used. Error bars represent the  $1\sigma$  Poisson sampling error in the mean. Positive values indicate that the angular momenta tend to point in the same direction, while negative values indicate that the angular momenta tend to point in opposite directions. The dotted line is the expected value for random orientations.

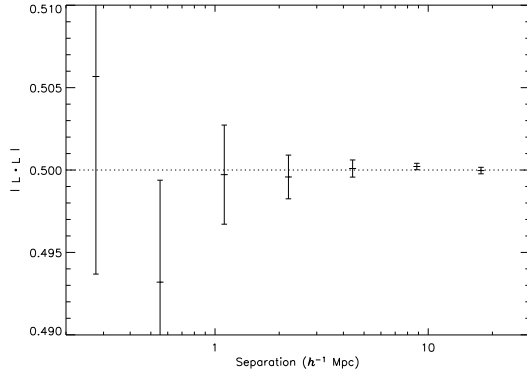


FIG. 32.— Mean correlation  $\xi_{|LL|}$  between the angular momentum vectors of halos as a function of their separation. All halos where the direction of the angular momentum is determined to within 0.4 radians are used. Error bars represent the  $1\sigma$  Poisson sampling error in the mean. Positive values indicate that the angular momentum vectors tend to lie parallel to each other, while negative values indicate that the angular momentum vectors tend to lie perpendicular. The dotted line is the expected value for random orientations.

angular momenta of other halos is defined as

$$\xi_{LL} \equiv \langle \hat{\mathbf{L}} \cdot \hat{\mathbf{L}} \rangle \equiv \frac{1}{N} \sum_{i,j} \hat{\mathbf{L}}_i \cdot \hat{\mathbf{L}}_j, \quad (16)$$

where the sum is over all unique pairs  $(i, j)$ . This is equivalent to the quantity defined as  $\eta(r)$  in Porciani et al. (2002a). As seen in Figure 31, we detect no deviations from random. We also measure the tendency for halo angular momentum vectors to be either parallel or perpendicular to each other. We define two quantities to measure this,

$$\xi_{|LL|} \equiv \langle |\hat{\mathbf{L}} \cdot \hat{\mathbf{L}}| \rangle \equiv \frac{1}{N} \sum_{i,j} |\hat{\mathbf{L}}_i \cdot \hat{\mathbf{L}}_j|, \quad (17)$$

which is the same as the quantity defined as  $\mu(r)$  in Hatton & Ninin (2001), and

$$\eta(r) \equiv \langle |\hat{\mathbf{L}} \cdot \hat{\mathbf{L}}|^2 \rangle - \frac{1}{3} \equiv \frac{1}{N} \sum_{i,j} |\hat{\mathbf{L}}_i \cdot \hat{\mathbf{L}}_j|^2 - \frac{1}{3}, \quad (18)$$

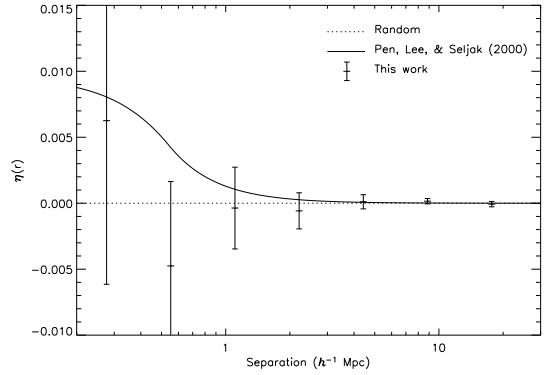


FIG. 33.— Correlation  $\eta(r)$  between the angular momentum vectors of halos as a function of their separation. All halos where the direction of the angular momentum is determined to within 0.4 radians are used. Error bars represent the  $1\sigma$  Poisson sampling error. Positive values indicate that the angular momentum vectors tend to lie parallel to each other, while negative values indicate that the angular momentum vectors tend to lie perpendicular. The dotted line is the expected value for random orientations. The solid line is the linear tidal torque prediction (Pen et al. 2000).

which is the same as Pen et al. (2000)'s  $\eta(r)$  and Porciani et al. (2002a)'s  $\eta_2(r)$ . The quantities  $\xi_{|LL|}(r)$  and  $\eta(r)$  are shown in Figures 32 and 33 respectively. We detect no deviations from isotropy. Due to the size of the error bars, these results are consistent with the non-detections and weak tendencies toward alignment found by other authors (Pen et al. 2000; Hatton & Ninin 2001; Porciani et al. 2002a; F02). We do not find any difference if we restrict the sample to halos of any particular mass range.

## 6. DISCUSSION

The differences between the properties of galaxy mass halos compared to those of group and cluster mass halos suggest that different factors determine their orientations. For example, the orientation of the major axis of a cluster is strongly affected by the direction of the most recently accreted subhalo, as seen in simulations (van Haarlem & van de Weygaert 1993; Tormen 1997) and observations (Ebeling, Barrett, & Donovan 2004). If these are accreted from filaments, then there should be a strong alignment of cluster principal axes with the filaments, as we have found. We find that the tendency of the minor axis to lie perpendicular to the filaments is much stronger than the tendency of the major axis to lie parallel to the filaments. While previous authors have neglected the minor axis, it appears that the effect of these mergers on the minor axis is stronger than their effect on the major axis. Another possibility is that the initial alignment of the major axis is stronger, but that figure rotation scrambles this alignment. Bailin & Steinmetz (2004) find that most halos show slow figure rotation about the minor axis, with a median pattern speed of  $0.15 h \text{ km s}^{-1} \text{ kpc}^{-1}$ , suggesting that the major axis of a typical halo can change by  $90^\circ$  in a Hubble time. The much weaker alignment for galaxy mass halos suggests that either the orientation of the axes is less affected by recent mergers (although Bailin & Steinmetz (2004) find no relationship between the pattern speed and halo mass, the lower mass halos are on average dynamically

older, and therefore figure rotation may have had a longer time to modify their orientation), or that the direction of the accretion is more isotropic (Vitvitska et al. 2002). Aubert et al. (2004) find that the accretion onto halos at masses down to  $5 \times 10^{12} M_{\odot}$  is quite anisotropic; however, 97% of our “galaxy” mass halos lie below this limit.

The differences between the angular momentum alignments for high and low mass halos are also intriguing. Angular momentum is usually thought to either arise from the tidal torquing of an asymmetric protohalo (White 1984), or by the accretion of substructure on non-radial orbits (Tormen 1997; Vitvitska et al. 2002). In a sense, these are not distinct scenarios; accreted subhalos *are* protogalactic material that has been tidally torqued. However, the relation between the direction of the angular momentum and surrounding matter may differ depending on the clumpiness of the accretion and other non-linear effects (Porciani et al. 2002a).

It is interesting to compare our results for collisionless dark matter halos with the results of Navarro et al. (2004) for simulations that include baryonic physics. The main results of Navarro et al. (2004) are that the angular momenta of baryonic galactic disks in gasdynamical simulations tend to align with the intermediate axis of the local baryon distribution on scales of  $\approx 2 h^{-1}$  Mpc, and that observed edge-on disk galaxies in the local supercluster have their spin axes lying within the supergalactic plane, as expected in this scenario. We find that on the scale of an individual halo, the angular momentum of the dark matter aligns with its minor axis. However, we find that the angular momentum of the dark matter in galaxy mass halos is parallel to the large scale structure, as expected if the spin vector lies within local sheet-like structures as suggested by Navarro et al. (2004). We also find that in low density regions, halo spins point toward nearby filaments, and are therefore aligned with the intermediate axis of the local density field. Therefore, despite the common presence of misalignments between the angular momenta of the baryons and the dark matter in individual galaxies (Sharma & Steinmetz 2004), each retains some memory of the large scale structure which provided the initial torques.

In the group and cluster mass halos, on the other hand, the angular momentum shows a strong tendency to point perpendicular to the large scale structure. These objects tend to occur at the intersections of large filaments, and have been built up by the recent accretion of smaller halos. These halos are accreted along the filaments, and therefore add angular momentum perpendicular to the filaments. This process appears to dominate the direction of the angular momentum for halos of mass greater than  $10^{13} h^{-1} M_{\odot}$ . Unlike for galaxy mass halos, for which we can confirm that the angular momenta of the dark matter and baryons share similar relationships to the large scale structure in simulations, we do not have high resolution gasdynamical simulations of these more massive objects with which to compare. It may be possible to determine the rotation axis of baryons in these systems observationally. In theory, the spin vector of a relaxed cluster can be deduced from the presence of a redshift gradient of the galaxies in the cluster; however, confusion due to structure along the line of sight, the small magnitude of the rotation compared to the intrinsic velocity dispersion, ambiguity in the orientation of the

ellipsoidal shape, intrinsic distance gradients, the lack of a large sample of substructureless relaxed clusters, and the uncertain relationship between the angular momentum of the cluster galaxies and that of the smooth X-ray emitting gas that dominates the baryonic mass make this measurement difficult. The rotation of the X-ray gas itself, however, may be measured using the kinematic Sunyaev-Zeldovich effect in future Cosmic Microwave Background (CMB) surveys (Chluba & Mannheim 2002; Cooray & Chen 2002).

## 7. SUMMARY

We have studied the internal shapes and angular momenta of galaxy and group mass dark matter halos formed in a  $\Lambda$ CDM  $N$ -body simulation, and studied how they are correlated with the large scale structure and the properties of neighbouring halos.

Internally, halos are triaxial with  $b/a$  and  $c/a$  ratios of  $0.75 \pm 0.15$  and  $0.6 \pm 0.1$  respectively. The distribution of axis ratios has a tail to low values. The two-dimensional projected ellipticities cover a broad range of values from 0 to 0.5, with a mean of 0.24. The axis ratios rise between  $0.12$  and  $0.6 r_{\text{vir}}$ , beyond which they drop. Within  $0.12 r_{\text{vir}}$ , the measurement is probably compromised by the force softening in the simulations. Halos are most often prolate in the inner regions, but tend to a more even mix of prolate and oblate at large radii.

The internal alignment of the halos within  $0.6 r_{\text{vir}}$  is very good, particularly for the minor axis, with a slight decrease in alignment in the outermost regions. High mass halos have particularly well-aligned axes. The orientation of the angular momentum is also relatively constant, though it changes more noticeably as a function of radius than do the axes. At any given radius, the angular momentum vector tends to be aligned with the minor axis and be perpendicular to the major axis. It also shows a weaker tendency to be perpendicular to the intermediate axis. The alignment between the angular momentum and the principal axes gets weaker at larger radii. The properties of the halo at  $0.4 r_{\text{vir}}$  are quite characteristic of their values at most other radii.

The minor axes of halos show a strong tendency to lie perpendicular to the filaments. As a consequence, the major (and, to a lesser degree, intermediate) axes tend to point along filaments. Figure rotation about the minor axis may be responsible for the smaller degree of major axis alignment. These alignments fall off with distance as a power law. In all cases, the alignment for group and cluster mass halos extends to much larger separations than for galaxy mass halos. The major axes show a weak correlation with those of other nearby halos. There is no robust detection of a correlation for the other axes.

The angular momenta of halos in low density environments tend to point toward local density enhancements, in agreement with the results of Kashikawa & Okamura (1992) for galaxies  $2 h^{-1}$  Mpc or more away from the local supergalactic plane. The angular momenta of galaxy mass halos show a weak tendency to point along filaments on scales up to  $3 h^{-1}$  Mpc, but those of group and cluster mass halos show a very strong tendency to point perpendicular to the filaments. We detect no correlations of the angular momentum directions of nearby halos with each other, but due to the size of the error bars, this is consistent with previous linear and  $N$ -body studies that predict

weak correlations. Comparisons with recent gasdynamical simulations and observations of edge-on disk galaxies in the local supercluster suggest that both the baryons and dark matter in galaxies share a memory of the orientation of the large scale structure that provided the initial torque. Groups and clusters, on the other hand, appear to acquire most of their angular momentum from the accretion of subhalos along filaments. This may be tested with large samples of galaxy redshifts within relaxed clusters, or by kinematic Sunyaev-Zeldovich studies

in future CMB experiments.

This work has been supported by grants from the U.S. National Aeronautics and Space Administration (NAG 5-10827), the David and Lucile Packard Foundation, the Bundesministerium für Bildung und Forschung (FKZ 05EA2BA1/8), and by the American Astronomical Society and the National Science Foundation in the form of an International Travel Grant.

## REFERENCES

- Aubert, D., Pichon, C., & Colombi, S. 2004, MNRAS, in press  
 Bailin, J. 2003, ApJ, 583, L79  
 Bailin, J., & Steinmetz, M. 2004, ApJ, in press, (astro-ph/0405442)  
 Barnes, J., & Efstathiou, G. 1987, ApJ, 319, 575  
 Binggeli, B. 1982, A&A, 107, 338  
 Brown, M. L., Taylor, A. N., Hambly, N. C., & Dye, S. 2002, MNRAS, 333, 501  
 Bullock, J. S. 2002, in “The shapes of galaxies and their dark halos”, Proceedings of the Yale Cosmology Workshop, New Haven, Connecticut, USA, 28-30 May 2001., ed. Priyamvada Natarajan (Singapore: World Scientific), 109  
 Bullock, J. S., Dekel, A., Kolatt, T. S., Kravtsov, A. V., Klypin, A. A., Porciani, C., & Primack, J. R. 2001, ApJ, 555, 240  
 Buote, D. A., Jeltema, T. E., Canizares, C. R., & Garmire, G. P. 2002, ApJ, 577, 183  
 Cabanela, J. E., & Dickey, J. M. 1999, AJ, 118, 46  
 Catelan, P., Kamionkowski, M., & Blandford, R. D. 2001, MNRAS, 320, L7  
 Chambers, S. W., Melott, A. L., & Miller, C. J. 2002, ApJ, 565, 849  
 Chluba, J., & Mannheim, K. 2002, A&A, 396, 419  
 Colberg, J. M., White, S. D. M., Jenkins, A., & Pearce, F. R. 1999, MNRAS, 308, 593  
 Cole, S., & Lacey, C. 1996, MNRAS, 281, 716  
 Cooray, A., & Chen, X. 2002, ApJ, 573, 43  
 Crittenden, R. G., Natarajan, P., Pen, U., & Theuns, T. 2001, ApJ, 559, 552  
 Croft, R. A. C., & Metzler, C. A. 2000, ApJ, 545, 561  
 Debattista, V. P., & Sellwood, J. A. 1999, ApJ, 513, L107  
 Doroshkevich, A. G. 1970, Astrofizika, 6, 581  
 Dubinski, J. 1992, ApJ, 401, 441  
 —. 1994, ApJ, 431, 617  
 Dubinski, J., & Carlberg, R. G. 1991, ApJ, 378, 496  
 Ebeling, H., Barrett, E., & Donovan, D. 2004, ApJ, 609, L49  
 Faltenbacher, A., Gottlöber, S., Kerscher, M., & Müller, V. 2002, A&A, 395, 1, (F02)  
 Flin, P. 1987, MNRAS, 228, 941  
 Franx, M., Illingworth, G., & de Zeeuw, T. 1991, ApJ, 383, 112  
 Frenk, C. S., White, S. D. M., Davis, M., & Efstathiou, G. 1988, ApJ, 327, 507  
 Gerhard, O. E. 1983, MNRAS, 202, 1159  
 Han, C., Gould, A., & Sackett, P. D. 1995, ApJ, 445, 46  
 Hatton, S., & Ninin, S. 2001, MNRAS, 322, 576  
 Heavens, A., Refregier, A., & Heymans, C. 2000, MNRAS, 319, 649  
 Helmi, A. 2004a, MNRAS, 351, 643  
 —. 2004b, ApJ, 610, L97  
 Heyl, J. S., Hernquist, L., & Spergel, D. N. 1994, ApJ, 427, 165  
 Hoekstra, H., Yee, H. K. C., & Gladders, M. D. 2004, ApJ, 606, 67  
 Holmberg, E. 1974, Arkiv for Astronomi, 5, 305  
 Ibata, R., Lewis, G. F., Irwin, M., Totten, E., & Quinn, T. 2001, ApJ, 551, 294  
 Jing, Y. P., & Suto, Y. 2000, ApJ, 529, L69  
 —. 2002, ApJ, 574, 538, (JS02)  
 Johnston, K. V., Law, D. R., & Majewski, S. R. 2004, ApJ, submitted  
 Kashikawa, N., & Okamura, S. 1992, PASJ, 44, 493  
 Kasun, S. F., & Evrard, A. E. 2004, ApJ, submitted, (astro-ph/0408056) (KE04)  
 Kazantzidis, S., Kravtsov, A. V., Zentner, A. R., Allgood, B., Nagai, D., & Moore, B. 2004, ApJ, 611, L73  
 Knebe, A., Gill, S. P. D., Gibson, B. K., Lewis, G. F., Ibata, R. A., & Dopita, M. A. 2004, ApJ, 603, 7  
 López-Corredoira, M., Betancort-Rijo, J., & Beckman, J. E. 2002, A&A, 386, 169  
 Lee, J., & Pen, U. 2000, ApJ, 532, L5  
 —. 2001, ApJ, 555, 106  
 Lee, J., & Suto, Y. 2003, ApJ, 585, 151  
 —. 2004, ApJ, 601, 599  
 Majewski, S. R., Law, D. R., Johnston, K. V., Skrutskie, M. F., & Weinberg, M. D. 2003, in “IAU Symposium 220: Dark Matter in Galaxies”, eds. S. Ryder, D. J. Pisano, M. Walker, and K. Freeman, (astro-ph/0311522)  
 Martínez-Delgado, D., Gómez-Flechoso, M. Á., Aparicio, A., & Carrera, R. 2004, ApJ, 601, 242  
 Natarajan, P., & Refregier, A. 2000, ApJ, 538, L113  
 Navarro, J. F., Abadi, M. G., & Steinmetz, M. 2004, ApJ, in press, (astro-ph/0405429)  
 Navarro, J. F., Frenk, C. S., & White, S. D. M. 1996, ApJ, 462, 563  
 Olling, R. P., & Merrifield, M. R. 2000, MNRAS, 311, 361  
 Onuora, L. I., & Thomas, P. A. 2000, MNRAS, 319, 614  
 Ostriker, E. C., & Binney, J. J. 1989, MNRAS, 237, 785  
 Pen, U., Lee, J., & Seljak, U. 2000, ApJ, 543, L107  
 Plionis, M. 1994, ApJS, 95, 401  
 Porciani, C., Dekel, A., & Hoffman, Y. 2002a, MNRAS, 332, 325  
 —. 2002b, MNRAS, 332, 339  
 Rhee, G. F. R. N., & Katgert, P. 1987, A&A, 183, 217  
 Sackett, P. D. 1999, in ASP Conf. Ser. 182: Galaxy Dynamics - A Rutgers Symposium, ed. D. Merritt, J. A. Sellwood, & M. Valluri, 393  
 Sackett, P. D., Rix, H., Jarvis, B. J., & Freeman, K. C. 1994, ApJ, 436, 629  
 Sarazin, C. L. 1986, Rev. Mod. Phys., 58, 1  
 Sharma, S., & Steinmetz, M. 2004, ApJ, submitted, (astro-ph/0406533)  
 Splinter, R. J., Melott, A. L., Linn, A. M., Buck, C., & Tinker, J. 1997, ApJ, 479, 632  
 Stark, A. A. 1977, ApJ, 213, 368  
 Struble, M. F., & Peebles, P. J. E. 1985, AJ, 90, 582  
 Tormen, G. 1997, MNRAS, 290, 411  
 Ulmer, M. P., McMillan, S. L. W., & Kowalski, M. P. 1989, ApJ, 338, 711  
 van den Bosch, F. C., Abel, T., Croft, R. A. C., Hernquist, L., & White, S. D. M. 2002, ApJ, 576, 21  
 van Haarlem, M., & van de Weygaert, R. 1993, ApJ, 418, 544  
 Vitvitska, M., Klypin, A. A., Kravtsov, A. V., Wechsler, R. H., Primack, J. R., & Bullock, J. S. 2002, ApJ, 581, 799  
 Warren, M. S., Quinn, P. J., Salmon, J. K., & Zurek, W. H. 1992, ApJ, 399, 405, (W92)  
 West, M. J., Jones, C., & Forman, W. 1995, ApJ, 451, L5  
 West, M. J., Villumsen, J. V., & Dekel, A. 1991, ApJ, 369, 287  
 White, S. D. M. 1984, ApJ, 286, 38  
 Zaritsky, D., Smith, R., Frenk, C. S., & White, S. D. M. 1997, ApJ, 478, L53